# Assimilation of Sentinel-1 Backscatter into a Land Surface Model with River Routing and Its Impact on Streamflow Simulations in Two Belgian Catchments

MICHEL BECHTOLD,[a] SARA MODANESI,[b] HANS LIEVENS,[a,c] PIERRE BAGUIS,[d] ISIS BRANGERS,[a] ALBERTO CARRASSI,[e,f,g] AUGUSTO GETIRANA,[j,h] ALEXANDER GRUBER,[i] ZDENKO HEYVAERT,[a] CHRISTIAN MASSARI,[b] SAMUEL SCHERRER,[a,i] STÉPHANE VANNITSEM,[d] AND GABRIELLE DE LANNOY[a]

[a] *Department of Earth and Environmental Sciences, KU Leuven, Leuven, Belgium*
[b] *Research Institute for Geo-hydrological Protection, National Research Council, Perugia, Italy*
[c] *Department of Environment, Ghent University, Ghent, Belgium*
[d] *Royal Meteorological Institute of Belgium, Brussels, Belgium*
[e] *Department of Meteorology, University of Reading, Reading, United Kingdom*
[f] *National Centre for Earth Observation, University of Reading, Reading, United Kingdom*
[g] *Department of Physics "Augusto Righi," University of Bologna, Bologna, Italy*
[h] *Hydrological Sciences Laboratory, NASA Goddard Space Flight Center, Greenbelt, Maryland*
[i] *Department of Geodesy and Geoinformation, TU Wien, Vienna, Austria*
[j] *Science Applications International Corporation, Greenbelt, Maryland*

(Manuscript received 30 October 2022, in final form 28 July 2023, accepted 11 September 2023)

ABSTRACT: Accurate streamflow simulations rely on good estimates of the catchment-scale soil moisture distribution. Here, we evaluated the potential of Sentinel-1 backscatter data assimilation (DA) to improve soil moisture and streamflow estimates. Our DA system consisted of the Noah-MP land surface model coupled to the HyMAP river routing model and the water cloud model as a backscatter observation operator. The DA system was set up at 0.01° resolution for two contrasting catchments in Belgium: (i) the Demer catchment dominated by agriculture and (ii) the Ourthe catchment dominated by mixed forests. We present the results of two experiments with an ensemble Kalman filter updating either soil moisture only or soil moisture and leaf area index (LAI). The DA experiments covered the period from January 2015 through August 2021 and were evaluated with independent rainfall error estimates based on station data, LAI from optical remote sensing, soil moisture retrievals from passive microwave observations, and streamflow measurements. Our results indicate that the assimilation of Sentinel-1 backscatter observations can partly correct errors in surface soil moisture due to rainfall errors and overall improve surface soil moisture estimates. However, updating soil moisture and LAI simultaneously did not bring any benefit over updating soil moisture only. Our results further indicate that streamflow estimates can be improved through Sentinel-1 DA in a catchment with strong soil moisture–runoff coupling, as observed for the Ourthe catchment, suggesting that there is potential for Sentinel-1 DA even for forested catchments.

SIGNIFICANCE STATEMENT: The purpose of this study is to improve streamflow estimation by integrating soil moisture information from satellite observations into a hydrological modeling framework. This is important preparatory work for operational centers that are responsible for producing the most accurate flood forecasts for the society. Our results provide new insights into how and where streamflow forecasting could benefit from high-spatial-resolution Sentinel-1 radar backscatter observations.

KEYWORDS: Streamflow; Hydrology; Soil moisture; Radars/Radar observations; Data assimilation; Land surface model

## 1. Introduction

The soil moisture antecedent to a storm event exerts a major control on how rainfall partitions at the soil surface into infiltration and surface runoff and also how quickly the fraction of infiltrating water redistributes in the soil to generate subsurface runoff (Torres 2002; Mirus and Loague 2013). As a result, a threshold behavior in the relationship between catchment-averaged soil moisture and streamflow has often been reported in which fast discharge responses to rainfall events dominate for higher antecedent soil moisture conditions (Penna et al. 2011; Radatz et al. 2013). Antecedent soil moisture can therefore be equally important as the rain rate for explaining the temporal variability of stormflow runoff coefficients, i.e., the ratio of event stormflow to event rainfall (Penna et al. 2011). Soil moisture is not only important before a storm event but also influences interstorm discharge

Supplemental information related to this paper is available at the Journals Online website: https://doi.org/10.1175/JHM-D-22-0198.s1.

Denotes content that is immediately available upon publication as open access.

*Corresponding author*: Michel Bechtold, michel.bechtold@kuleuven.be

*Publisher's Note:* This article was revised on 11 December 2023 to apply the open access designation that was missing when originally published.

DOI: 10.1175/JHM-D-22-0198.1

processes that are, for example, controlling low flow periods. The soil moisture of deeper layers is often connected to the groundwater level, which is a major water source for streamflow during interstorm periods (Winter 2007; Zomlot et al. 2015).

For these reasons, accurate estimates of soil moisture are considered crucial to improve streamflow forecasting (Berthet et al. 2009; Tramblay et al. 2010). Since the advent of satellite-based soil moisture observations, model-based estimates of soil moisture have been regularly enhanced through data assimilation (DA) approaches (de Rosnay et al. 2014; Reichle et al. 2017a; De Lannoy et al. 2022). Satellite-based soil moisture DA has also been combined with streamflow modeling, and a number of studies demonstrated the potential of improving streamflow estimates (Pauwels et al. 2001; Wanders et al. 2014; Albergel et al. 2017; Cenci et al. 2017; Liu et al. 2018; De Santis et al. 2021; Reichle et al. 2021). In these studies, streamflow estimates did not improve consistently for all catchments and all streamflow periods. This can be expected, however, because the impact of soil moisture prediction errors on streamflow depends on several conditions. For example, for the more extreme rain events, rainfall errors are considered to dominate the errors in the fast runoff component, which, consequently, diminishes the impact of antecedent soil moisture simulations (Mao et al. 2019). Furthermore, the impact of soil moisture DA is already limited to some extent by the DA setup itself. Mao et al. (2019) suggested that soil moisture DA approaches that solely aim to reduce random errors (such as the widely used Kalman filter) are not optimal for streamflow corrections in catchments where random errors account for only a relatively small portion of the total error. Similarly, Fairbairn et al. (2017) considered model deficiencies and model nonlinearities as major reasons that DA did not lead to improvements of streamflow estimates in their setup. Indeed, Crow et al. (2018) found that the land surface models seem to generally underestimate soil moisture–runoff coupling, which will reduce potential positive impacts of soil moisture DA. The DA impact can also be reduced due to a low surface to root-zone layer coupling that prevents root-zone moisture updates (Chen et al. 2011) and, therefore, reduces alterations to the rainfall–runoff transformation. Further, Loizu et al. (2018) found that the impact of soil moisture DA on streamflow is sensitive to the applied model structure. In their results, improvements were greater for a physically based model than for a conceptual model, which might be related to a more direct link between the soil moisture variable in the model and the satellite soil moisture retrieval.

The assimilation of vegetation information to improve soil moisture and eventually streamflow estimates is less well documented but has untapped potential for many reasons. For example, the assimilation of leaf area index (LAI) or vegetation optical depth has the potential to improve root-zone soil moisture (RZSM) estimates (Sabater et al. 2008; Kumar et al. 2019, 2021; Xu et al. 2021) and thus to strengthen the effect of surface soil moisture retrieval assimilation. Furthermore, improved vegetation estimates may lead to improved simulation of rainfall interception. However, so far, only few studies have explored simultaneous soil moisture and vegetation updating using retrieval products, and these studies reported only neutral to slightly positive impacts on streamflow estimation (Albergel et al. 2017; Fairbairn et al. 2017).

The above studies investigated the potential of assimilating optical or microwave-based satellite retrieval products of soil moisture or vegetation for streamflow estimation. It is also possible to update soil moisture and vegetation by directly assimilating microwave signals. The assimilation of retrievals suffers from inconsistencies with respect to the used models, which may reduce the potential positive impacts of the data assimilation. Instead, a calibrated observation operator might allow disentangling the combined soil moisture and vegetation information contained, for example, in multiangular or multipolarized passive or active microwave observations (De Lannoy and Reichle 2016a; Vreugdenhil et al. 2018; Modanesi et al. 2022).

This paper aims to exploit the potential of improving streamflow estimates with a recently developed setup for the assimilation of active microwave backscatter observations from Sentinel-1 (Modanesi et al. 2022). The DA setup differs from earlier studies focused on streamflow estimation through soil moisture updating in that we directly use the raw satellite signal (instead of retrievals) to update either soil moisture alone or soil moisture and LAI simultaneously, using an observation operator and an ensemble Kalman filter. Furthermore, observations are used at a rather fine resolution (Sentinel-1 observations processed to 0.01°) which should help to improve the spatial pattern of soil moisture and the associated streamflow estimates (Pauwels et al. 2001). The impact of the assimilation and the two updating modes is assessed in detail for two catchments in Belgium, one dominated by agriculture and with low topographic gradients and one mainly covered with mixed forests and with higher topographic gradients. Note that the setup investigated in this paper is still focused on the correction of random errors and thus intended to contribute to the existing body of literature on improving streamflow through soil moisture and vegetation state updating.

The paper is organized as follows. In section 2, we present the two study catchments, the used datasets, and the DA system. In section 3, we present the results of an analysis of the DA diagnostics, and of an evaluation of the DA output against rainfall error estimates and independent reference data of soil moisture and LAI, and eventually streamflow measurements. In section 4, we discuss the reasons for the observed differences between DA experiments and catchments. In section 5, we provide conclusions and suggestions for future research.

## 2. Study area and data

### a. Study area

We selected two catchments with contrasting properties in Belgium for our study: the Demer catchment and the Ourthe catchment. Figure 1 shows their location as well as maps of topography, drainage area, soil texture, and land cover. Details about the sources of the geographic data are given in section 2b.

The Demer catchment covers an area of 1775 km$^2$ and is characterized by low topographic gradients. The land-cover fractions are 60% cropland, 23% forests, 14% urban and built-up, and 3% grassland. The cropland is mainly located on sandy loam, while the forests are mainly on sand. The remaining silt loam has a mixed land cover. During the study period

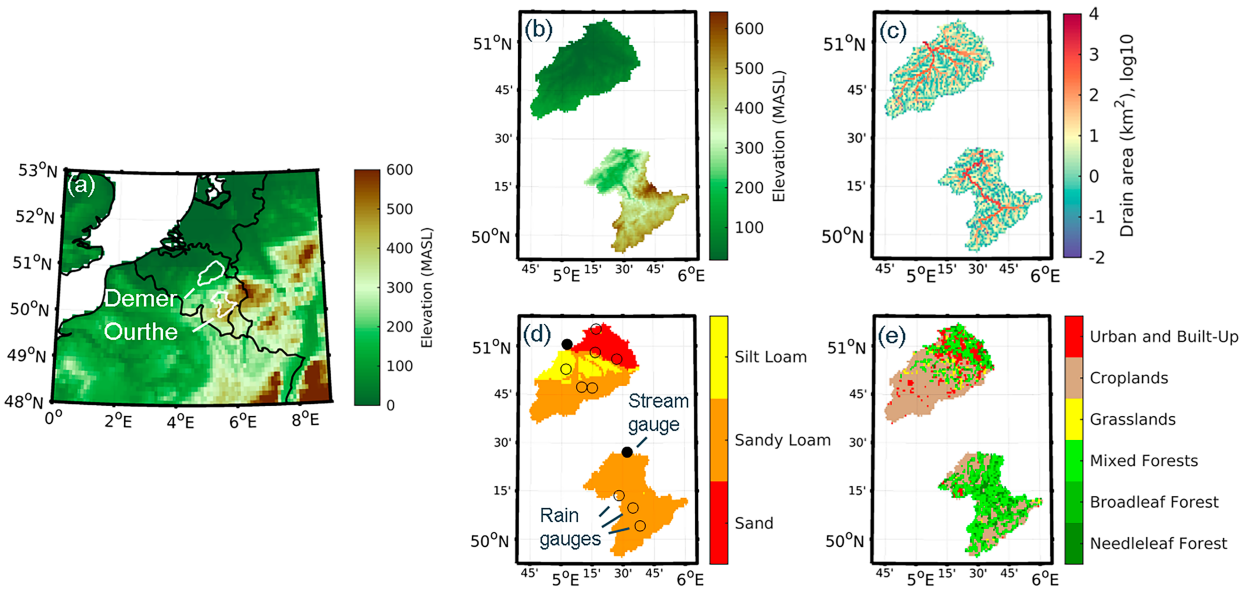


FIG. 1. (a) Locations of the two study catchments Demer and Ourthe in Belgium, and their spatial distributions of (b) elevation, (c) drainage area, (d) soil texture, and (e) land cover.

(2015 through 2020), the Demer catchment has an annual mean temperature of 11°C and a mean annual precipitation of 693 mm. Irrigation plays a minor role in the agriculture of the Demer catchment.

The Ourthe catchment covers an area of 1616 km$^2$. It is located in the Ardennes and features higher topographic gradients. The land-cover fractions are 64% forests, 34% cropland, 1% grassland, and 1% urban and built-up. The Ourthe catchment consists entirely of sandy loam soils. The Ourthe catchment had a mean annual temperature of 9.3°C and a mean annual precipitation of 808 mm and is thus slightly colder and wetter than the Demer catchment due to mild orographic effects. Like the Demer, also, the Ourthe is mainly rainfed.

### b. Data

#### 1) GEOGRAPHIC DATA

The following geographic data were used in the land surface modeling and river routing:

- Land-cover type of NASA's Moderate Resolution Imaging Spectroradiometer (MODIS; Friedl et al. 2002) using the University of Maryland (UMD) land-cover classification (Hansen et al. 2000);
- Soil texture of the Harmonized World Soil Database 1.21 (FAO/IIASA/ISRIC/ISSCAS/JRC 2012) with a weighted combination of surface and subsurface texture to derive a homogeneous root zone for the land surface model as in De Lannoy et al. (2014);
- Elevation of the NASA's Shuttle Radar Topography Mission (SRTM; Farr et al. 2007);
- River flow directions were derived from the Multi-Error-Removed Improved-Terrain (MERIT; Yamazaki et al. 2017) digital elevation model (DEM) at 3-arc-s spatial resolution. MERIT DEM is based on SRTM processed with successive correction of absolute bias, stripe noise, speckle noise, and tree height bias from using multiple satellite datasets and filtering techniques.

#### 2) STREAMFLOW DATA

Streamflow data were available at the catchment outlets (Fig. 1d) in Molenstede for the Demer and in Tabreux for the Ourthe. Quality-controlled daily streamflow (m$^3$ s$^{-1}$) was obtained from www.waterinfo.be and https://hydrometrie.wallonie.be and converted into millimeters per day (mm day$^{-1}$) using the catchment area. Neither catchment includes significant water reservoirs, and the time series are thus largely free of water management effects.

#### 3) METEOROLOGICAL DATA

Meteorological data used as input to the land surface model include precipitation, air temperature, surface pressure, specific humidity, incoming shortwave radiation, incoming longwave radiation, and wind speed and direction. The dynamic meteorological forcings were extracted from the Modern-Era Retrospective Analysis for Research and Applications, version 2 (MERRA-2; Gelaro et al. 2017), at hourly resolution. Here, we used the rain gauge-corrected precipitation of MERRA-2 (Reichle et al. 2017b). The meteorological data were downscaled to 0.01° using bilinear interpolation and a lapse-rate topographic forcing correction (Cosgrove et al. 2003).

To assess whether soil moisture updates are linked as expected to possible forcing data errors, we estimated the error of the reanalysis precipitation data by calculating the difference between catchment-averaged reanalysis precipitation and station-based precipitation. Regionally available rain gauge data

(Fig. 1d) from www.waterinfo.be and https://hydrometrie.wallonie.be were regridded on the modeling grid using nearest neighbor and then averaged over each catchment.

#### 4) SENTINEL-1 SATELLITE DATA

The Sentinel-1 mission of the European Space Agency (ESA) and Copernicus collects active microwave backscatter data at the C band (5.4 GHz) at a high spatial (5 m × 20 m) resolution in an interferometric wide swath (IW) mode. The Sentinel-1 mission includes two satellites, *Sentinel-1A* and *Sentinel-1B*. They follow the same orbits with a time difference of 6 days. For the study area, the temporal resolution of observations for each satellite is approximately 4 days. Over the period in which both satellites were active (i.e., from September 2016 through August 2021, corresponding to the end of the study period), this resulted in a 2-day temporal resolution.

The processing of the ground-range detected (GRD) IW backscatter observations in VV and VH polarization was done similarly as in Lievens et al. (2022) using the ESA Sentinel Application Platform (SNAP) software and included standard techniques: precise orbit file application, border noise removal, thermal noise removal, radiometric calibration to backscatter as beta nought, terrain flattening to backscatter as gamma nought ($\gamma^0$: $\gamma^0$VV, $\gamma^0$VH), and range-Doppler terrain correction. Furthermore, $\gamma^0$ observations, originally acquired at ~20-m spatial resolution, over water bodies, and built-up areas were filtered out and then aggregated to the 0.01° latitude–longitude grid of the land surface model by averaging in linear scale. Observations from different relative orbits can be biased relative to each other due to incidence angle and azimuthal effects which we accounted for by calibrating the observation operator for each relative orbit separately (section 3b). In total, the study area was covered by five different relative orbits of which two had an ascending and three a descending track. Prior to the observation operator calibration and the DA, the 0.01° observations were masked for periods of frozen soil and snow cover based on the land surface model ice fraction (>0.0001 $m^3$ $m^{-3}$) and snow water equivalent (>0.001 m). Note that we did not mask for dense vegetation and instead allowed the calibrated observation operator to optimally disentangle the combined soil moisture and vegetation information contained in the Sentinel-1 observations.

#### 5) REMOTELY SENSED REFERENCE DATA

We evaluated the surface soil moisture (SFSM) and LAI from the DA experiments against remotely sensed reference data. Note that, in our DA setup, Sentinel-1 backscatter is assimilated and not soil moisture retrievals and LAI. For SFSM, we selected a passive microwave-based retrieval product which comes with the caveat of also being based on microwave observations but is supposed to minimize error correlations with the soil moisture and vegetation signal extracted from active microwave data from Sentinel-1. We used the SFSM retrievals from the NASA Soil Moisture Active Passive (SMAP) mission from April 2015 onward. More specifically, the Enhanced L2 Radiometer Half-Orbit 9 km EASE-Grid Soil Moisture, version 4 (SPL2SMP_E), product was used (Chan et al. 2018; Chaubell et al. 2020). From this product, we used the retrieval of the single-channel algorithm using vertical polarization (soil moisture option 2) which is the baseline for SMAP soil moisture in the version 4 product. The quality flag for dense vegetation was relaxed to allow an evaluation over the forested catchment. Specifically, we included retrievals that were obtained for a vegetation water content between 5 and 30 kg $m^{-2}$. Even though retrievals are likely of poorer quality, they still allow for assessing relative differences in the performance of the different experiments.

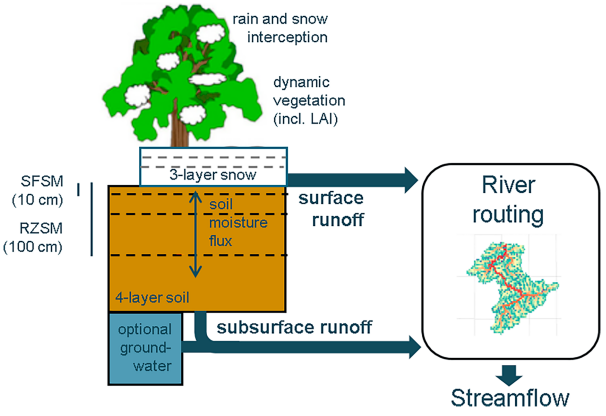


FIG. 2. Schematic overview of the hydrological modeling setup consisting of the land surface model Noah-MP, version 3.6, coupled to the HyMAP river routing. SFSM: surface soil moisture; RZSM: root-zone soil moisture; LAI: leaf area index.

As a reference for LAI, we used the satellite LAI product derived from the Project for On-Board Autonomy–Vegetation (PROBA-V) and Satellite Pour l'Observation de la Terre–Vegetation (SPOT-VGT) missions (Verger et al. 2014), obtained from the Copernicus Global Land Service (CGLS). It has a 10-day resolution and is composed of images from an adaptive window of 15–60 days, depending on the available valid measurements. Here, we used the 300-m-resolution product which was regridded to the 0.01° model grid by spatial averaging.

## 3. Methodology

### a. *Land surface model and river routing*

Figure 2 shows a schematic overview of the hydrological modeling setup consisting of a land surface model and a river routing component. For the land surface model, we used the Noah multiparameterization (Noah-MP) model (Niu et al. 2011), version 3.6, which is an extension to the Noah land surface model (Chen et al. 1996) through the incorporation of multiple and new physics capabilities. The advanced physics in Noah-MP includes, among other options, multilayer snowpack, multiple options for surface water infiltration, runoff, and groundwater including the representation of an unconfined water table depth as a lower boundary condition (Niu et al. 2007). In our study, we simulated soil moisture in the following four layers: 0–10, 10–40, 40–100, and 100–200 cm.

Noah-MP also includes a dynamic vegetation model which is of key importance for our study by allowing for the prognostic representation of vegetation growth and senescence. The

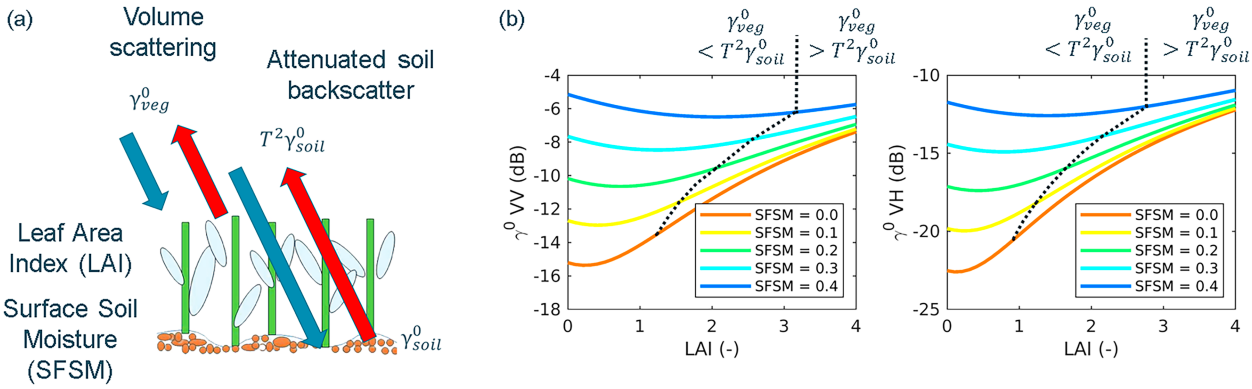


FIG. 3. (a) Schematic illustration of the water cloud model and its two backscatter ($\gamma^0$) components "volume scattering" and "attenuated soil backscatter" and (b) the relationship between $\gamma^0$VV and $\gamma^0$VH and the two input parameters, LAI ($m^2\ m^{-2}$) and SFSM ($m^3\ m^{-3}$), for an exemplary set of calibrated water cloud model parameters. The dashed line indicates the LAI for which volume scattering equals the amount of attenuated soil $\gamma^0$.

dynamic vegetation model combines the Ball–Berry photosynthesis-based stomatal resistance model (Ball et al. 1987) with the dynamic vegetation model of Dickinson et al. (1998). The carbon storage in the leaf, stem, wood, and root parts are prognostic vegetation state variables that allow the vegetation state updating by assimilating vegetation-sensitive satellite observations such as LAI (Kumar et al. 2019). Noah-MP also has an interception module in which the canopy capacity for rain and snowfall interception is calculated as a function of LAI and stem area index with land-cover specific parameters.

The gridcell surface and subsurface runoff fields from Noah-MP were then used as input to the Hydrological Modeling and Analysis Platform (HyMAP; Getirana et al. 2012, 2017) streamflow routing model which routed the input through a prescribed river network and eventually generated estimates of routed streamflow at the outlets of the two catchments. HyMAP is a state-of-the-art global-scale hydrodynamic model capable of simulating surface water dynamics, including water storage, elevation, and discharge in-stream, as well as in floodplains. HyMAP can simulate water dynamics in rivers and floodplains using different methods to solve the full momentum equation of open channel flow (local inertia formulation; Getirana et al. 2017). Here, we adopted the kinematic wave equation as this option has been demonstrated to hold also for relatively flat catchments (Moramarco et al. 2008). The Courant–Friedrichs–Lewy (CFL) condition is used to determine HyMAP's optimal sub–time steps for numerical stability. Rivers and floodplains interact laterally and have independent flow dynamics, with roughness and geometry derived from land-cover characteristics, topography, and river parameterization (Getirana et al. 2012; Getirana and Peters-Lidard 2013). HyMAP is run over the same model grid as the land surface model. Note that a possible feedback from the routing model to the land surface model moisture state variables (e.g., Getirana et al. 2021) was not modeled for simplicity because, given the absence of significant floodplains, such a feedback is of minor importance for the study area (Decharme et al. 2019; Getirana et al. 2021).

We refrained from tuning any model parameters in Noah-MP and HyMAP to mimic a later application over multiple, including ungauged, catchments. All model parameters were kept at the default values typically applied in other studies. However, we made one exception for the lower boundary condition. As discussed in Fairbairn et al. (2017), a decent model performance is important to enable streamflow improvements through data assimilation. We noticed substantial biases in streamflow with the default option and thus tested all four available Noah-MP lower boundary options, including the groundwater options, to obtain a reasonable open-loop performance over both catchments. The Demer catchment was eventually simulated with the TOPMODEL groundwater option with an equilibrium water table (Niu et al. 2005) and the Ourthe catchment with a free drainage option (Dickinson et al. 1993).

### b. Observation operator

The assimilation of $\gamma^0$ data requires the implementation of an observation operator (also referred in variational DA literature as a forward operator), in order to map the prognostic state variables to the observation space (De Lannoy et al. 2022). The water cloud model (WCM) (Attema and Ulaby 1978) is the most established observation operator for $\gamma^0$ data (Lievens et al. 2017; Modanesi et al. 2021). It assumes that the vegetation layer can be approximated as a water cloud of randomly distributed equally sized water droplets that scatter and attenuate radiation. Figure 3a shows a schematic illustration of the water cloud model.

The total $\gamma^0$ is modeled as the sum (in linear scale) of two $\gamma^0$ components:

$$\gamma^0 = \gamma^0_{\text{veg}} + T^2\gamma^0_{\text{soil}}, \tag{1}$$

with $\gamma^0_{\text{veg}}$ being the volume scattering in the vegetation layer in linear scale (—) and $\gamma^0_{\text{soil}}$ being the soil $\gamma^0$ in linear scale (—) reduced by the attenuation parameter $T^2$. Here, $T^2$ is computed as a function of LAI,

$$T^2 = \exp(-2 \times B \times \text{LAI}), \tag{2}$$

in which $B$ is a dimensionless model parameter. Note that Eq. (2) is a simplification of the original water cloud model in which $T^2$ also depends on incidence angle. We implicitly accounted for this incidence angle dependency, however, by using terrain flattened backscatter data $\gamma^0$ and also calibrated the water cloud model

separately for each relative orbit; $B$ is therefore absorbing the remaining incidence angle effect from different travel lengths through the vegetation layer. The vegetation scattering is also simulated as a function of LAI:

$$\gamma^0_{\text{veg}} = A \times \text{LAI}(1 - T^2), \tag{3}$$

with $A$ being another dimensionless model parameter. As in Eq. (2), incidence angle effects are, in this study, absorbed in $A$. Previous research indicated that the soil $\gamma^0$ in dB scale often linearly depends on volumetric SFSM (Ulaby et al. 1978) leading to

$$\gamma^0_{\text{soil}} = C + D \times \text{SFSM}, \tag{4}$$

with $C$ (dB) and $D$ [dB $(\text{m}^3\ \text{m}^{-3})^{-1}$] being two model parameters describing the intercept and slope of the relationship.

Like the classical Kalman filter for linear dynamics, the ensemble-based Kalman filter used as DA approach in this study assumes unbiased observations and forecasts (Reichle et al. 2002). Therefore, in order to mitigate or in the best scenario remove the biases, the four parameters $A$, $B$, $C$, and $D$ were calibrated for each pixel, relative orbit, and polarization separately using a Bayesian function with a prior parameter penalty term as described in Modanesi et al. (2021). The parameters were calibrated with SFSM and LAI from a deterministic Noah-MP simulation and the processed 0.01° Sentinel-1 observations of the full study period. The optimization was done with the shuffled complex evolution algorithm (Duan et al. 1993).

Prior parameter constraints were chosen as in Modanesi et al. (2021) with the exception of the $D$ parameter. For our study area, we found that the resulting simulated $\gamma^0$ time series, after calibration, strongly underestimated the short-term variability in response to soil moisture changes visible in the Sentinel-1 observations. One reason for this might be that the strong seasonal negative cross correlation between soil moisture and LAI (at monthly averages $R = -0.73$) prevented the system from properly separating soil moisture and vegetation-related information in the water cloud model parameters. We thus implemented an alternative approach to better constrain the prior information for the slope parameter $D$ [Eq. (4)]. In this approach, the prior best guess value of $D$ was estimated (for each relative orbit, pixel, and polarization) by fitting a linear model to data points of $\gamma^0_{t2} - \gamma^0_{t1}$ and $\text{SFSM}_{t2} - \text{SFSM}_{t1}$ with t1 and t2 being two consecutive time steps of the same relative orbit and polarization. The fitted slope of the linear model represents the short-term dependency of $\gamma^0$ on SFSM and was determined for the 6 months with the lowest simulated LAI. The slope was taken as prior best guess, and prior parameter boundaries were reduced to ±5 dB $(\text{m}^3\ \text{m}^{-3})^{-1}$. Resulting performance metrics and WCM parameters are shown for the three orbits with full coverage in the online supplemental material (Figs. S1–S9). The performance of the WCM slightly varied across orbits and land-cover types. We found that the sensitivity to soil moisture, as indicated by the correlation between $\gamma^0_{t2} - \gamma^0_{t1}$ and $\text{SFSM}_{t2} - \text{SFSM}_{t1}$, was often slightly lower over forests than over cropland and grassland. Nevertheless, the correlation values also indicated a useful sensitivity to soil moisture over forests in particular for the time period of the 50% lowest LAI values (Fig. S10). The observation operator was applied in the data assimilation without any additional data masking.

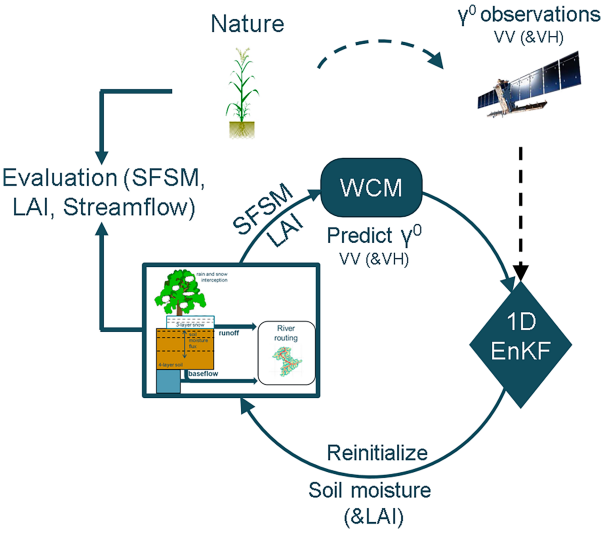


FIG. 4. Overview of the data assimilation system. SFSM and LAI dynamically simulated by Noah-MP are fed into a calibrated observation operator (WCM) to estimate Sentinel-1 $\gamma^0$ in VV (and VH). A one-dimensional ensemble Kalman filter (1D EnKF) updates soil moisture in different layers (and LAI) using Sentinel-1 $\gamma^0$VV (and $\gamma^0$VH) observations. Experiments are evaluated against SFSM and LAI reference datasets and measured streamflow.

By using this stronger constraint on $D$ in the calibration of the WCM parameters, the WCM is supposed to better attribute short- and long-term backscatter changes to changes in soil moisture and LAI. Indeed, we obtained better subsequent DA results with this approach than when using weak constraints on all parameters (not shown).

Figure 3b illustrates the dependency of $\gamma^0$VV and $\gamma^0$VH on SFSM and LAI for an exemplary grid cell as modeled by the water cloud model. First, $\gamma^0$VH typically concerns much smaller values than $\gamma^0$VV. Next, it can be seen that for low LAI values, the attenuation effect of vegetation dominates over the volume scattering effect, leading to reduced $\gamma^0$ with increasing LAI. For higher LAI, both increasing SFSM and increasing LAI lead to increases in $\gamma^0$. The dashed line in each subplot indicates the LAI at which $\gamma^0$ from volume scattering equals the attenuated soil $\gamma^0$. For most pixels, the dashed line was shifted to the left for VH when compared to VV indicating the higher sensitivity of VH to the vegetation layer (Vreugdenhil et al. 2018).

### c. *Data assimilation system*

Figure 4 gives an overview of the DA system that was implemented into NASA's Land Information System (LIS; Kumar et al. 2006; Peters-Lidard et al. 2007). The land model consisting of a land surface model and a water cloud model predicts $\gamma^0$ in VV and VH polarization for each relative orbit and polarization. The assimilation is performed

TABLE 1. Perturbation parameters for the forcing variables rainfall, and incident and shortwave radiation, and the modeled state variables surface soil moisture (SFSM) and leaf area index (LAI). The perturbation type was either additive or multiplicative, with the standard deviation given for a normal or lognormal distribution, respectively.

| Variable | Perturbation type | Standard deviation |
|---|---|---|
| Rainfall (kg $m^{-2}$ $s^{-1}$) | Multiplicative | 0.5 |
| Incident longwave radiation (W $m^{-2}$) | Additive | 50.0 |
| Incident shortwave radiation (W $m^{-2}$) | Multiplicative | 0.3 |
| SFSM ($m^3$ $m^{-3}$) | Additive | 0.012 |
| LAI ($m^2$ $m^{-2}$) | Additive | 0.04 |

with a one-dimensional (1D; considering just vertical error correlations) ensemble Kalman filter (EnKF; Reichle et al. 2002) which sequentially updates the land surface state with every incoming Sentinel-1 $\gamma^0$ observation ($\gamma^0$VV or $\gamma^0$VH, or both). In our DA experiments, the updated land surface state variables included either only the four simulated soil moisture layers (experiment name "DASM," see Fig. 3), if only $\gamma^0$VV was assimilated, or both the four soil moisture layers and LAI ("DASMLAI"), if $\gamma^0$VV and $\gamma^0$VH were assimilated jointly. For the latter, one single sample error covariance was calculated between all forecasted land surface states (SM and LAI) and both forecasted $\gamma^0$ polarizations; i.e., each polarization updated all state variables. The updated LAI from assimilation is also used to update the prognostic leaf biomass by dividing the LAI value by the constant land-cover-dependent specific leaf area consistent with the Noah-MP physics formulations (Liu et al. 2016). Other vegetation mass prognostic variables in Noah-MP related to the stem, wood, and root mass are not updated, same as in the LAI data assimilation in Kumar et al. (2019).

All other flux and state variables are adjusted via model propagation. The DA system corresponds to the one used in Modanesi et al. (2022) except that here we assimilated data from each relative orbit individually with separately calibrated WCM parameter values and at the corresponding relative orbit overpass time (descending at 0600 LT, ascending at 1800 LT). Tests showed a slight performance improvement for the orbit-specific DA (not shown).

Proper estimates of forecast and observation errors are crucial for the optimality of a Kalman filter setup. The observation error standard deviation is supposed to represent both measurement error and errors of the observation operator (van Leeuwen 2015; Janjić et al. 2018). After calibration of the water cloud model, the root-mean-squared deviation (RMSD) between modeled and observed $\gamma^0$ was on average approximately 1 dB with little difference between polarizations and relative orbits. We considered 1 dB as the upper limit of the observation error since the RMSD also includes errors in the input variables (SFSM and LAI) to the water cloud model. The uncertainty in both input variables is likely substantial, e.g., due to the coarse meteorological forcing and the typically high uncertainty in vegetation models. Based on performance in test runs with differently reduced observation error standard deviation, we eventually decided for 0.7 dB for the two polarizations and all relative orbits.

In an EnKF, the forecast errors are diagnosed from an ensemble of land model simulations, here represented by 24 ensemble members. Larger ensemble sizes used in a testing phase (not shown) had a marginal impact on our results, suggesting that the EnKF is already very close to its asymptotic skill achievable when the ensemble size tends to infinity. The ensembles are generated by perturbing selected meteorological input forcings and state variables. The applied perturbation parameters are summarized in Table 1 and follow Modanesi et al. (2022). Those parameters led, on average, to a unit standard deviation of normalized $\gamma^0$ observation-minus-forecast residuals (or innovations) which is often used as an indicator for optimal assimilation diagnostics (De Lannoy and Reichle 2016b; Reichle et al. 2017a). To avoid the introduction of biases through perturbations, the perturbation bias-correction algorithm of Ryu et al. (2009) was applied in all our ensemble simulations. We verified for our modeling setup that the bias correction effectively removed biases in the ensemble mean of soil moisture and LAI relative to the deterministic simulation.

### d. *Experiments and evaluation approach*

We conducted three different ensemble simulation experiments: one open loop (OL; no DA) and two DA experiments. The experiments were the following:

- Open loop (OL): Ensemble model-only simulation, with gridcell surface and subsurface runoff routed using HyMAP to compute streamflow
- Data assimilation with soil moisture updating (DASM): DA of $\gamma^0$VV for updating soil moisture only, and with HyMAP river routing
- Data assimilation with soil moisture and LAI updating (DASMLAI): DA of $\gamma^0$VV and $\gamma^0$VH for simultaneous updating of soil moisture and LAI, and with HyMAP river routing

The initial conditions for the land surface model were generated by conducting a model spinup in which the model was run in deterministic mode twice from 1981 until 31 March 2014. The model is then started in ensemble mode on 1 April 2014 using the conditions of the end of the spinup. The experiments were evaluated over January 2015–August 2021.

The evaluation of the experiments is divided into two parts:

The first part focuses on the evaluation of the DA system. This includes (i) a spatial evaluation of the absolute $\gamma^0$ observation-minus-forecast ($O - F$) residuals and SFSM and LAI increments (difference of pre- and postupdate) to analyze their dependency on land surface properties, (ii) an analysis of the relationship between precipitation errors and SFSM

increments, and (iii) a spatial evaluation of SFSM and LAI against independent remotely sensed reference data using time series Pearson correlation coefficients $R$.

The second part focuses on the impact of the DA on streamflow. We evaluated streamflow at two different levels. First, we calculated skill metrics for the full streamflow time series. Specifically, we determined the Kling–Gupta efficiency index (KGE; Gupta et al. 2009) between simulated and measured streamflow as well as its analog based on the square root of the streamflow (KGEsq) which reduces the weight of the peak flow periods (De Santis et al. 2021). The KGE (and KGEsq) has become a widely used metric for evaluating the goodness of fit in hydrological modeling studies and measures the bias, correlation, and difference in variance between time series. The skill metric ranges between $-\infty$ and 1 (optimal value). Second, we evaluated skill at the level of storm events. We based this analysis on the separation of the daily time series into discrete 6-day storm event periods as done by Crow et al. (2018). We also used a precipitation threshold of 5 mm for the storm event identification. This threshold needs to be exceeded at the first day of each event period but must not occur in the coming 5 days to avoid the interference of multiple events. Any storm event must also be preceded by at least a single day with a daily precipitation amount below this threshold. To separate the total flow of each event into the baseflow and stormflow, we applied the hydrograph separation algorithm HYSEP (Sloto and Crouse 1996). We evaluated the experiments on their skill in estimating the total flow of storm events and additionally the stormflow-only component of storm events. Since the EnKF is not supposed to correct for long-term biases, the event-based evaluation was based on the Pearson correlation coefficient instead of KGE.

## 4. Results

### a. Evaluation of the data assimilation setup

#### 1) Data assimilation diagnostics

Figure 5 shows the spatial distribution of the temporal standard deviation of the observation-minus-forecast [std($O - F$)] $\gamma^0$ residuals for the OL and the two different DA experiments for January 2015–August 2021. The mean of the std($O - F$) of the OL is 1.01 dB for VV and 1.11 dB for VH. The DA introduces a reduction in std($O - F$) by 0.24 to 0.30 dB for the two experiments and two polarizations. The reduction of the std ($O - F$) in VV is 0.06 dB stronger when $\gamma^0$VH is also assimilated.

The spatial pattern of std($O - F$) in the Demer catchment shows a connection to the spatial distribution of soil texture and land cover (see Fig. 1). The highest std($O - F$) can be observed for the croplands on sandy loam soil in the south of the Demer catchment. This area also features the highest reductions in std($O - F$) after DA. Furthermore, the Demer catchment shows an aerial fraction of 14% over which the Sentinel-1 observations were flagged for urban and built-up land cover. For the Ourthe catchment, there is nearly full spatial coverage of observations, but a lower temporal coverage (especially during the winter, not shown) due to more frozen conditions.

Figure 6 shows the spatial distribution of the time series standard deviation of the increments of SFSM [std(ΔSFSM)], RZSM [std(ΔRZSM)], and, in the experiment DASMLAI, also for LAI [std(ΔLAI)]. On average, the std[ΔSFSM] in the DASM experiment was 0.006 $m^3\ m^{-3}$ and about 3 times higher than std(ΔRZSM) indicating an expected decrease of increments with soil depth. The joint use of $\gamma^0$VV and $\gamma^0$VH in the DASMLAI experiment slightly increased both std(ΔSFSM) and std(ΔRZSM) when compared to the DASM experiment in which only $\gamma^0$VV was used. The std(ΔLAI) in the DASMLAI experiment was 0.057.

In line with the spatial patterns of std($O - F$), the spatial patterns in soil moisture and LAI increments show a relation to soil texture and land-cover patterns. The largest increments are again found for the croplands on sandy loam in the south of the Demer catchment. For the Ourthe catchment, the highest increments in soil moisture also occur over cropland areas in the northwestern and southeastern parts.

A large fraction of soil moisture increments is supposed to be connected to antecedent errors in precipitation (Reichle et al. 2021). We tested whether we observe this connection too in our Sentinel-1 DA setup. Figure 7 shows all ΔSFSM calculated one day after an event with a large precipitation error. The precipitation error was computed as the difference between the daily MERRA-2 precipitation $P_{M2}$ and the catchment-averaged station-based precipitation $P_S$. A large error was defined as an absolute error of at least 1 mm $day^{-1}$ and a relative error of at least 10% of the average of $P_{M2}$ and $P_{S2}$ of that day. Over the Demer and Ourthe catchments, we found that the slope of the linear fit between ΔSFSM and $P_{M2} - P_S$ is significant at the 0.001 level in the Demer catchment (DASM: $p = 1.2 \times 10^{-5}$; DASMLAI: $p = 1.3 \times 10^{-6}$) and at the 0.05 level in the Ourthe catchment (DASM: $p = 0.04$; DASMLAI: $p = 0.03$) with only a minor difference between the two DA setups. This confirms that overestimated $P_{M2}$ in the model forecast is indeed corrected at the analysis time step by withdrawing water from the soil (negative ΔSFSM), and vice versa in case of underestimated $P_{M2}$. Note that the remaining scatter is caused by several factors such as time-lagged effects of earlier precipitation errors, the magnitude of the rain event itself, observation operator errors, and errors in the precipitation error estimates.

#### 2) Evaluation against reference data: Soil moisture and leaf area index

Figure 8 shows the spatial distribution of the Pearson anomaly correlation (anomR) between the time series of SFSM from the different experiments and the independent (i.e., not assimilated) SFSM retrievals from SMAP ($SFSM_{SMAP}$). For both DA setups, anomR increased compared to the OL experiment run over almost the entire study domain (i.e., in both catchments). An exception was the area of sandy soil texture in the Demer catchment where the DA had little effect. The average increase in anomR was 0.08 for the DASM experiment and 0.06 for the DASMLAI experiment. The spatial pattern of improvements was nearly identical in both DA experiments.

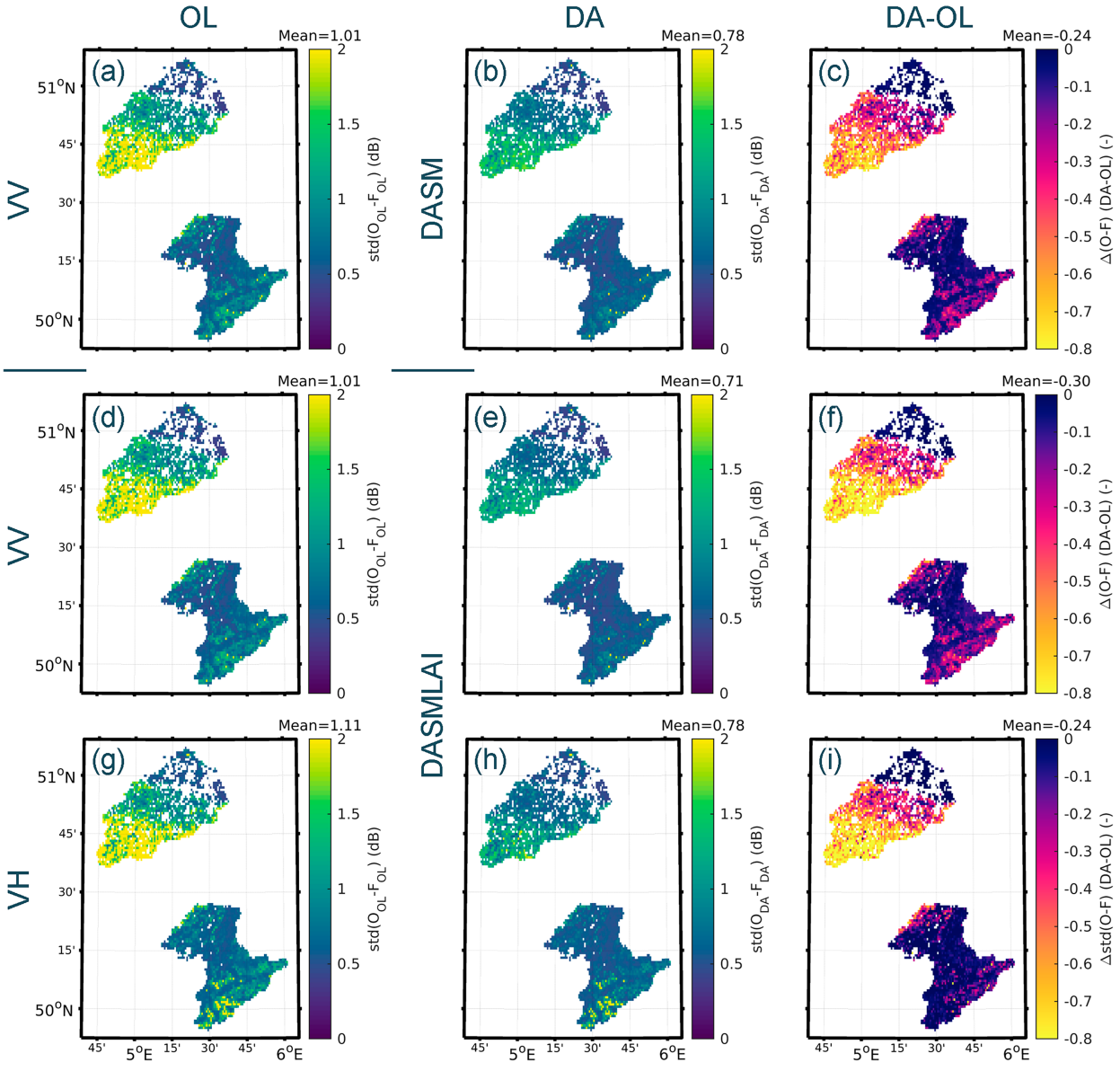


FIG. 5. Time series standard deviation of $\gamma^0$ residuals [std($O - F$)] for (a),(d),(g) the open loop (OL) and data assimilation (DA) of the (b) DASM and (e),(h) DASMLAI experiments, and (c),(f),(i) the difference between DA and OL. Note that (d) is identical to (a) and was repeated for readability.

Figure 9 shows the spatial distribution of anomR between the time series of LAI from the different experiments and the independent (not assimilated) LAI from CGLS. On average, the DA barely changed anomR in the DASM experiment ($\Delta$anomR $= -0.001$), but strong regional differences occurred. While the effect of soil moisture updates on LAI was relatively strong (both improving and deteriorating anomR) over croplands, it was minor over forests. The additional impacts on LAI through direct LAI updating can be seen in the results of the DASMLAI experiment. Here, rather consistent improvements in anomR can be seen over the croplands in the Demer catchment, while deterioration occurred over the croplands in the Ourthe catchment. For the forests, a slight but largely consistent deterioration can be observed. Averaged over both domains, anomR decreases by $-0.016$ through DA for the DASMLAI experiment.

Figures 10 and 11 show several catchment-averaged time series for the Demer and Ourthe catchments. Due to the strong similarity between the two DA experiments, time series are only shown for the DASMLAI experiment. The corresponding figures for the DASM experiment are provided in the supplement (Figs. S11 and S12). SFSM, RZSM, LAI, and streamflow time series from both the OL and DA experiments are shown together with independent measurements of streamflow and reference data for SFMC and LAI from SMAP and CGLS, respectively.

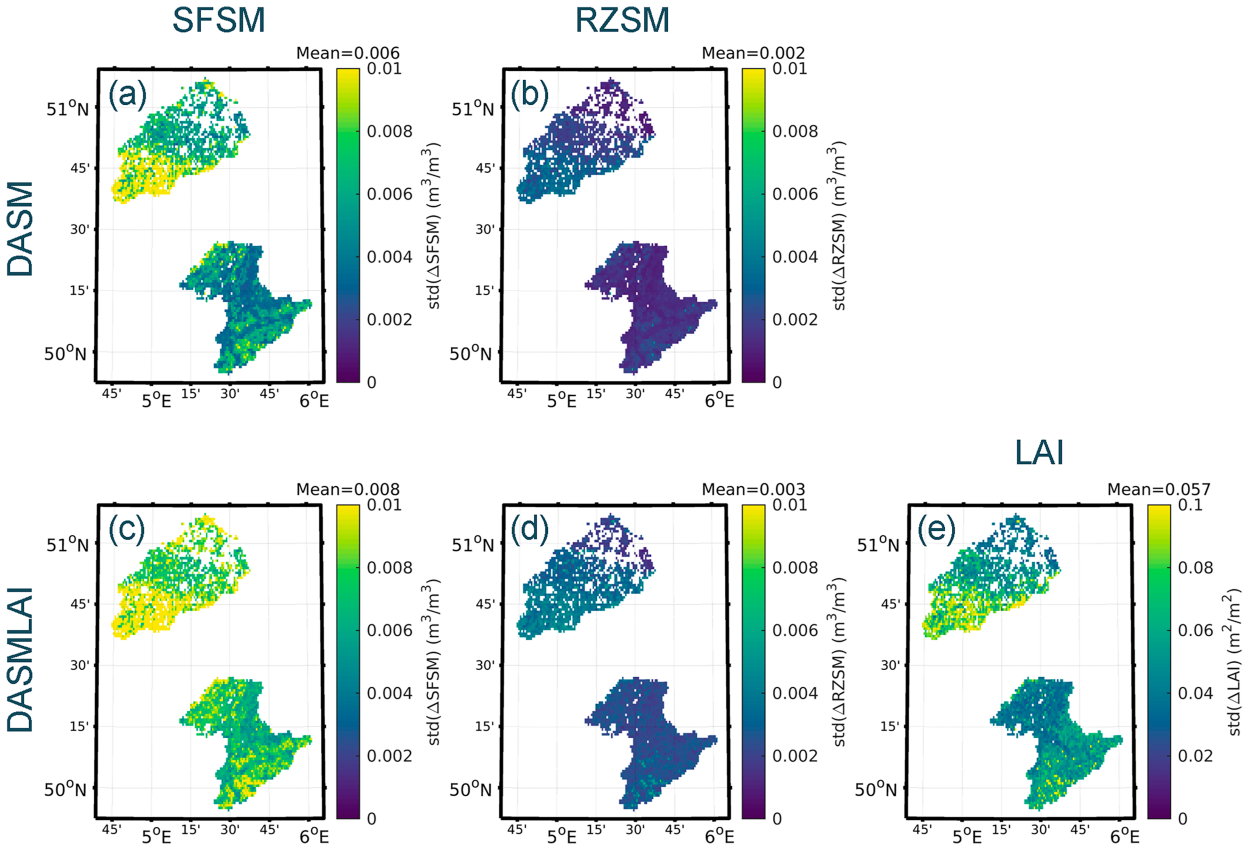


FIG. 6. Time series standard deviation of increments in (a),(c) surface soil moisture (ΔSFSM), (b),(d) root-zone soil moisture (ΔRZSM), and (e) LAI (ΔLAI, for DASMLAI only) of the (top) DASM and (bottom) DASMLAI experiments.

For the Demer catchment, several periods can be observed in which the assimilation of Sentinel-1 $\gamma^0$ led to stronger drydowns during April/May than in the OL experiment, most clearly visible in 2018 and 2020. The stronger drydowns correspond well to the drydowns in the SMAP reference data. The time series of RZSM show that these SFSM drydowns also propagate into the deeper soil layers. For the same period, the DA shows a substantially reduced LAI (which is also visible in the DASM experiment; Figs. S11 and S12).

For the Ourthe catchment, differences in catchment-averaged SFSM, RZSM, and LAI between the OL and DA are generally smaller than over the Demer catchment. In contrast to the Demer catchment, the DA over the Ourthe does not result in stronger drydowns in April/May.

### b. *Streamflow evaluation*

#### 1) KLING–GUPTA EFFICIENCY INDEX

The assimilation of Sentinel-1 $\gamma^0$ also induced changes in streamflow through model propagation. Table 2 shows the KGE and KGEsq computed over all daily streamflow data pairs in January 2015–August 2021 for all experiments. For the two DA experiments, an improvement relative to the OL experiment could only be found for the Ourthe catchment for which KGE and KGEsq both increased by 0.03 in both the DASM and DASMLAI experiments. The improvements are small when integrated over all seasons of the whole multiyear time series, but temporary large improvements can be seen, e.g., at the end of 2017 for the Ourthe catchment (Fig. 11). For the Demer, KGE and KGEsq did not change in the DASM experiment, while in the DASMLAI experiment, the impact on KGE was negative and neutral on KGEsq.

#### 2) EVENT STREAMFLOW EVALUATION

Figure 12 focuses on the end of 2017 mentioned previously for the Ourthe catchment and illustrates the impact of soil moisture updating on streamflow during two exemplary storm events. The RZSM and SFSM of the DA experiment were 0.02 and 0.015 $m^3\ m^{-3}$ higher than those of the OL experiment, respectively, which substantially increased total flow as well as the stormflow component, in particular for "event 2." Figure 12 also shows that the model simulates the peak flows of those two events with a delay of approximately 2 days compared to the measured streamflow.

The streamflow amounts of all identified storm events in the Demer ($n$ = 88) and Ourthe ($n$ = 72) catchments were used for further evaluation. Figure 13 shows the KGE and the Pearson correlation $R$ between the modeled event streamflow and observed event streamflow for the total flow, and the

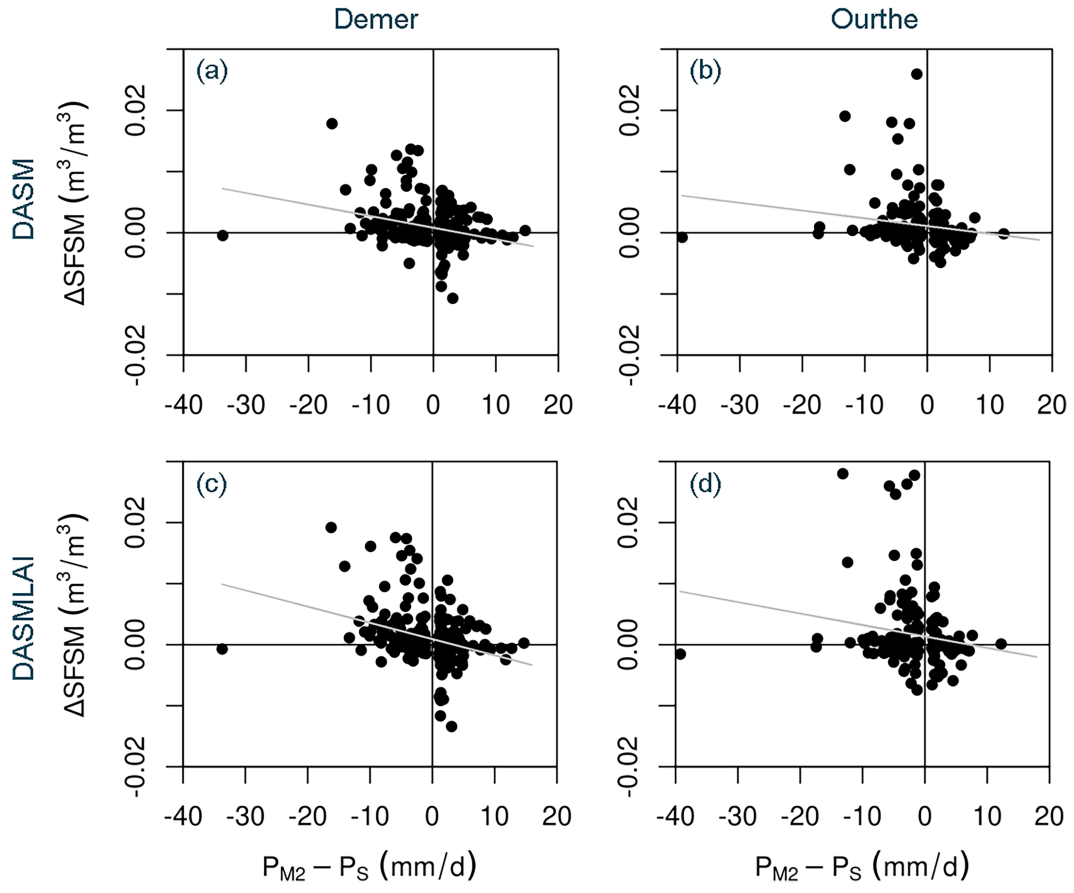


FIG. 7. Catchment-averaged increments of ΔSFSM as a function of the precipitation error of the previous day estimated by the difference between MERRA-2 precipitation $P_{M2}$ and station precipitation $P_S$ for the (a),(c) Demer and (b),(d) Ourthe catchments for the two different data assimilation experiments. The gray line in each plot indicates the linear regression.

baseflow and stormflow components individually. At the level of event streamflow amounts, a minor improvement in $R$ can be observed for the Demer catchment for both DA experiments, while the impact on KGE was rather neutral. For the Ourthe catchment, $R$ more clearly improved by about 0.05 in both DA experiments, and nearly equally for the total flow, and the baseflow and the stormflow components individually. However, also for the Ourthe, changes to the KGE were minor.

## 5. Discussion

### a. *Impact of Sentinel-1 backscatter assimilation on soil moisture and LAI in the Noah-MP model*

Our analyses indicate that soil moisture from the Noah-MP model can be improved through Sentinel-1 $\gamma^0$ DA over both catchments. Slightly greater improvements can be observed over croplands compared to forests, which is expected since the $\gamma^0$ sensitivity to soil moisture decreases with increasing thickness of the vegetation layer. The main correction of soil moisture occurred both (i) in response to rainfall errors, as illustrated by the relationship between SFSM increments and precipitation errors derived from station data, and (ii) also during drydown periods as indicated by the correspondence with independent SFSM retrievals from SMAP.

The updates during the drydown periods over croplands in April and May, however, need to be interpreted with caution. April/May is the period in which the shoots of several crops grow upward. Due to a predominantly vertical vegetation structure, very abrupt declines in VV polarization over only a few weeks were reported, e.g., over winter wheat fields (Schlund and Erasmi 2020). Similar effects might occur for barley and maize which are, besides winter wheat, frequent crops in the Demer catchment. The WCM approximates the effects of the vegetation water content on backscatter using the "water cloud" concept. Specific vegetation structural effects are not accounted for as this would require a more complex model with more parameters (Quast and Wagner 2016) that is hard to calibrate with uncertain soil moisture and vegetation inputs from land surface modeling. It is possible that this simplification of the WCM led to partly unrealistic state updates in April/May through $\gamma^0$VV assimilation as also reported in Modanesi et al. (2022). The transition from almost bare soil to a vegetation cover with elongated

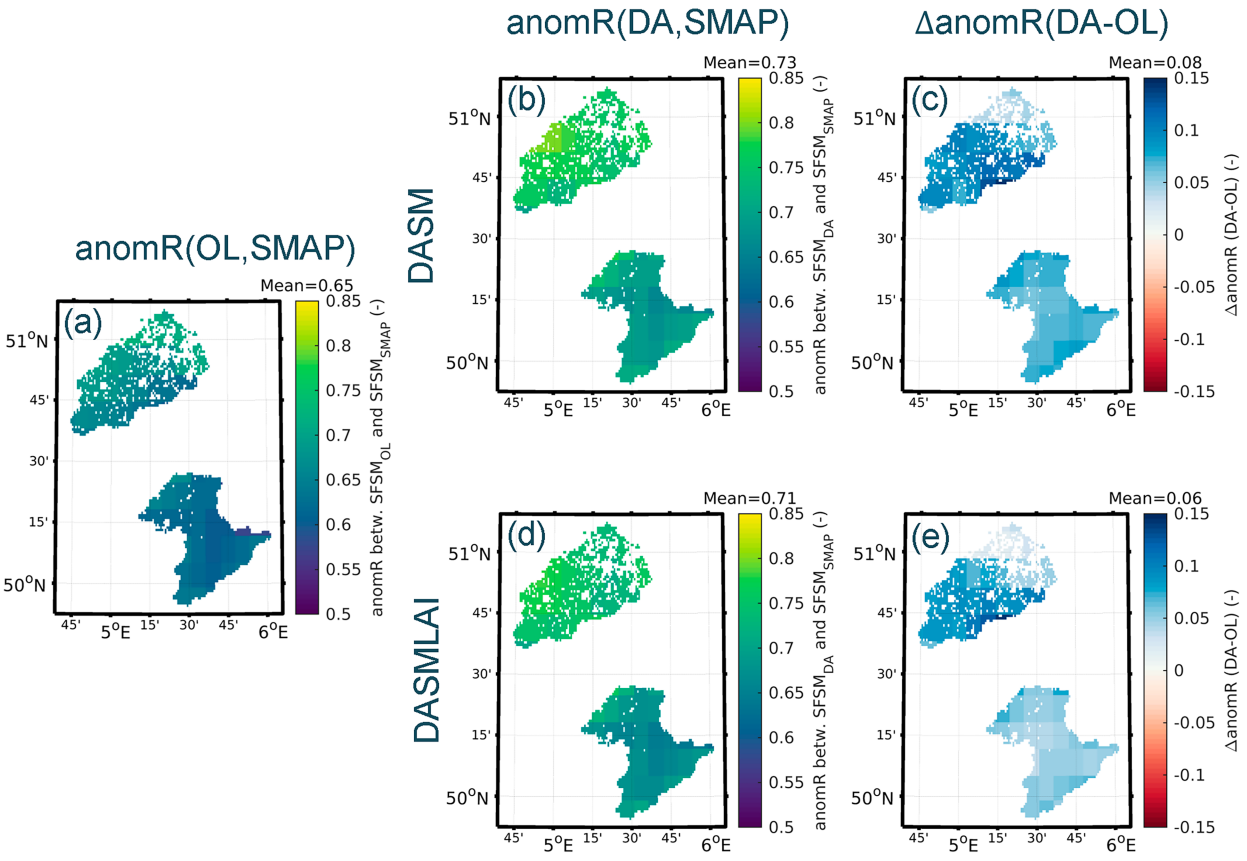


FIG. 8. Pearson anomaly correlation coefficient anomR between modeled and SMAP level-2 SFSM for the (a) open loop (OL) and DA of the (b) DASM and (d) DASMLAI experiments, and (c),(e) the corresponding difference between DA and OL.

plant structures during crop shooting might also have an impact on the soil moisture retrievals from passive microwave remote sensing (Wigneron et al. 2007, 2017) which could explain the good correspondence between the surface soil moisture of the DA time series and the independent SMAP soil moisture retrievals.

There are other factors impacting the poor performance of the water cloud model over croplands as indicated by the largest std($O - F$) seen in Fig. 5. While a forest does not change a lot from year to year, agricultural lands do, e.g., due to tillage practices and crop rotation. Since our DA setup worked with time-constant water cloud model parameters, the filter might not know the "right" partitioning between vegetation and soil updates in the DASMLAI experiment. Similarly, in the DASM experiment, std($O - F$) might be used for soil moisture updating although they originated from vegetation effects.

Regardless of whether soil moisture improved or not over croplands, the soil moisture increments of the DASM experiment degraded LAI relative to the independent CGLS LAI data. The time series of both DA experiments over the Demer catchment (Fig. 10 and Fig. S11) show that the drier soil moisture causes a substantially reduced LAI due to modeled plant water stress. During this same period, the LAI of the DA deviates most from the reference LAI because the impact of plant water stress is likely overestimated in the April/May period. Without additional data, it cannot be ascertained whether this LAI error is due to a possibly deteriorated soil moisture after DA in April/May or errors in the modeling of the plant physiology.

The comparison of the DASM and DASMLAI experiments reveals only a minor additional impact on LAI in the DASMLAI experiment, both in the correlation with CGLS LAI (Fig. 9) and in LAI time series (Fig. 10 and Fig. S11). This is surprising because there were substantial LAI increments (mean absolute increment of 0.06 $m^2$ $m^{-2}$). As discussed in depth by Scherrer et al. (2022), this is likely partly due to the structure of the vegetation model in Noah-MP which has an intrinsic model equilibrium state depending on the vegetation-type specific parameters. If the updated vegetation state significantly deviates from the model equilibrium (associated with the current soil water availability, which is partly determined by soil parameters), the updates do not sufficiently persist. Instead, the model drifts back toward its original state (Dee 2005; De Lannoy et al. 2007). This behavior of the Noah-MP vegetation model also explains that the spread in LAI is not widening with increasing LAI (Fig. 10); i.e., the vegetation model does not further propagate the uncertainty. Instead, the model drift of each ensemble member back toward the model equilibrium state causes the spread to shrink.

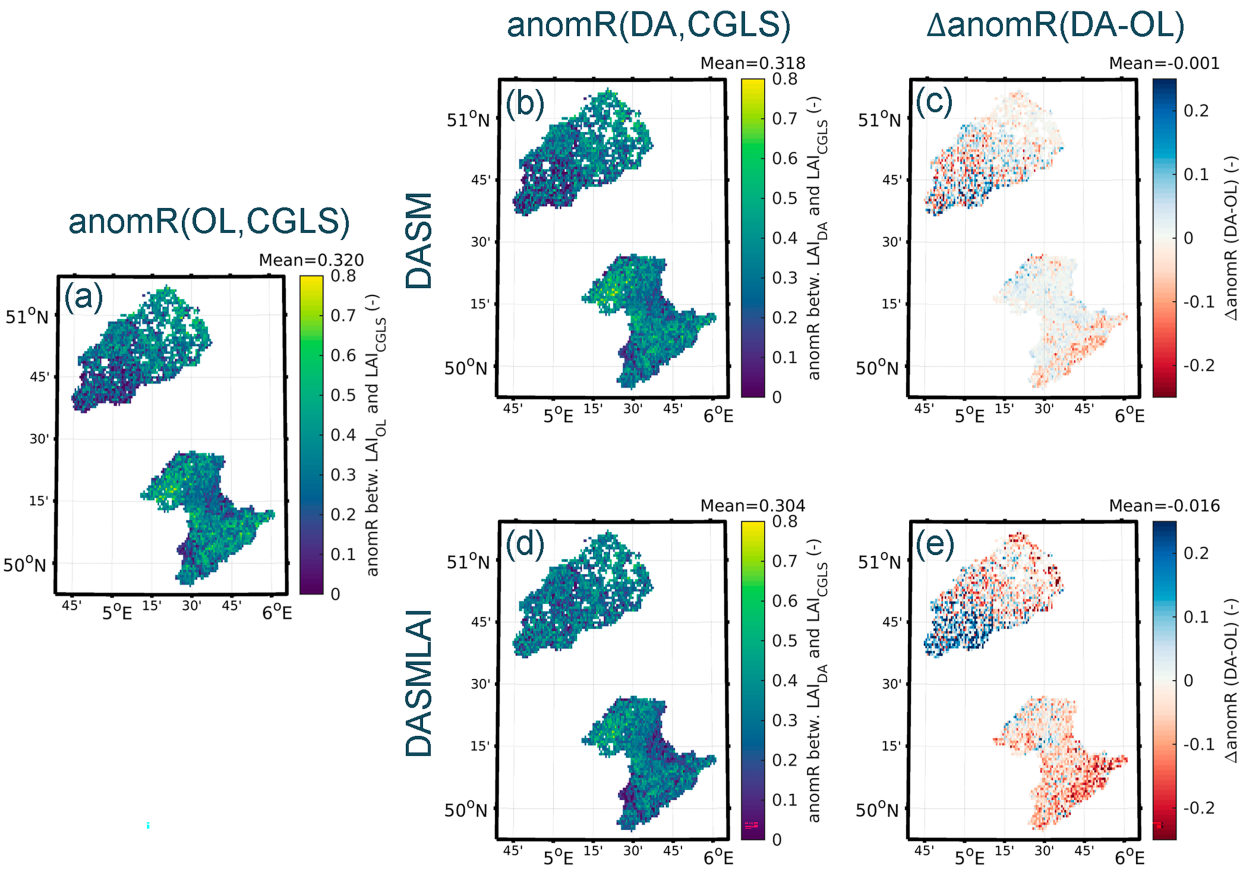


FIG. 9. Pearson anomaly correlation coefficient anomR between modeled and CGLS LAI for the (a) OL and DA of the (b) DASM and (d) DASMLAI experiments and (c),(e) the corresponding difference between DA and OL.

### b. *Catchment dependency of the DA impact on streamflow*

Our study showed that Sentinel-1 $\gamma^0$ improved the streamflow estimation only for one of the two catchments. Perhaps surprisingly, this was the Ourthe catchment for which soil moisture updates were smaller and where a high forest fraction would typically be considered as problematic to extract the soil moisture signal from microwave observations due to vegetation structure effects (Vreugdenhil et al. 2020). Furthermore, more frequent snow covers and higher snow depths (Fig. 11) led to more masked Sentinel-1 observations and also subsequent snowmelt events which could thus not be improved by Sentinel-1 DA.

The DA improved the streamflow for the Ourthe catchment in terms of the KGE and KGEsq of the full daily time series as well as for a storm event–based evaluation in terms of Pearson correlation coefficients. In contrast, the DA impact on streamflow was overall neutral for the Demer catchment. The event-based evaluation proved to be a useful evaluation method to reduce the role of model deficiencies and model nonlinearities in evaluating DA impacts which were considered as problematic in earlier studies (e.g., Fairbairn et al. 2017). The two exemplary storm events of Fig. 12 illustrate how soil moisture substantially modified the streamflow response in terms of streamflow amounts, but not much in terms of peak flow timing. The latter is only slightly shifted by DA but still mainly depends on the parameters of the land surface model and river routing. If the peak flow timing is still predicted poorly, improving the magnitude of peak flow does not necessarily improve skill at a daily resolution. In contrast, improvements will become apparent when evaluating at the time-aggregation level of storm events. This may explain that, for the Demer catchment, a degradation of streamflow through DA was not observed in the event-based evaluation and not for the KGEsq which lowers the impact of peaks, while, in contrast, the KGE indicated a degradation for the DASMLAI experiment (Table 2). Note also that delays due to the routing are more critical in the Demer catchment than in the Ourthe catchment due to the lower topographic gradients.

To better understand if streamflow processes in one of the two catchments are naturally more sensitive to soil moisture than in the other, we analyzed the soil moisture–runoff coupling strength. As done in Crow et al. (2018), we calculated the Spearman rank correlation coefficient between antecedent soil moisture and the runoff coefficient. Antecedent soil moisture was determined based on the driest of the 2 days preceding a storm event, and the runoff coefficient was computed as either the total streamflow or the stormflow only divided by the total precipitation amount during the storm event. The runoff coefficient was either based on station-based observations of precipitation and

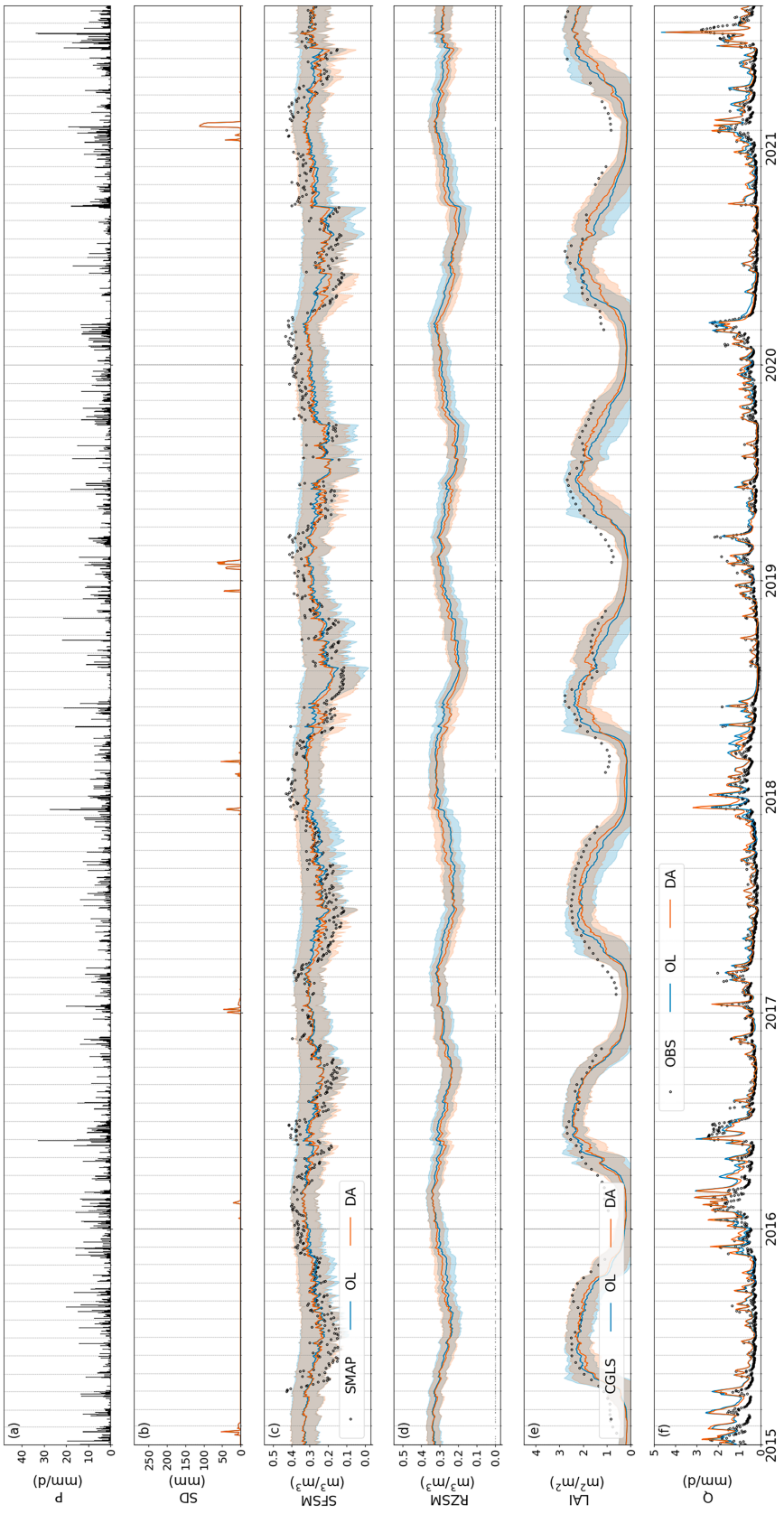


FIG. 10. Time series of the DASMLAI experiment for the Demer catchment of catchment-averaged (a) precipitation $P$, (b) snow depth (SD), (c) SFSM, (d) RZSM, (e) LAI, and (f) streamflow $Q$. Light colored shading in (c), (d), and (e) indicates the ensemble spread. The distribution of assimilated Sentinel-1 observations is shown as black dots in (d).

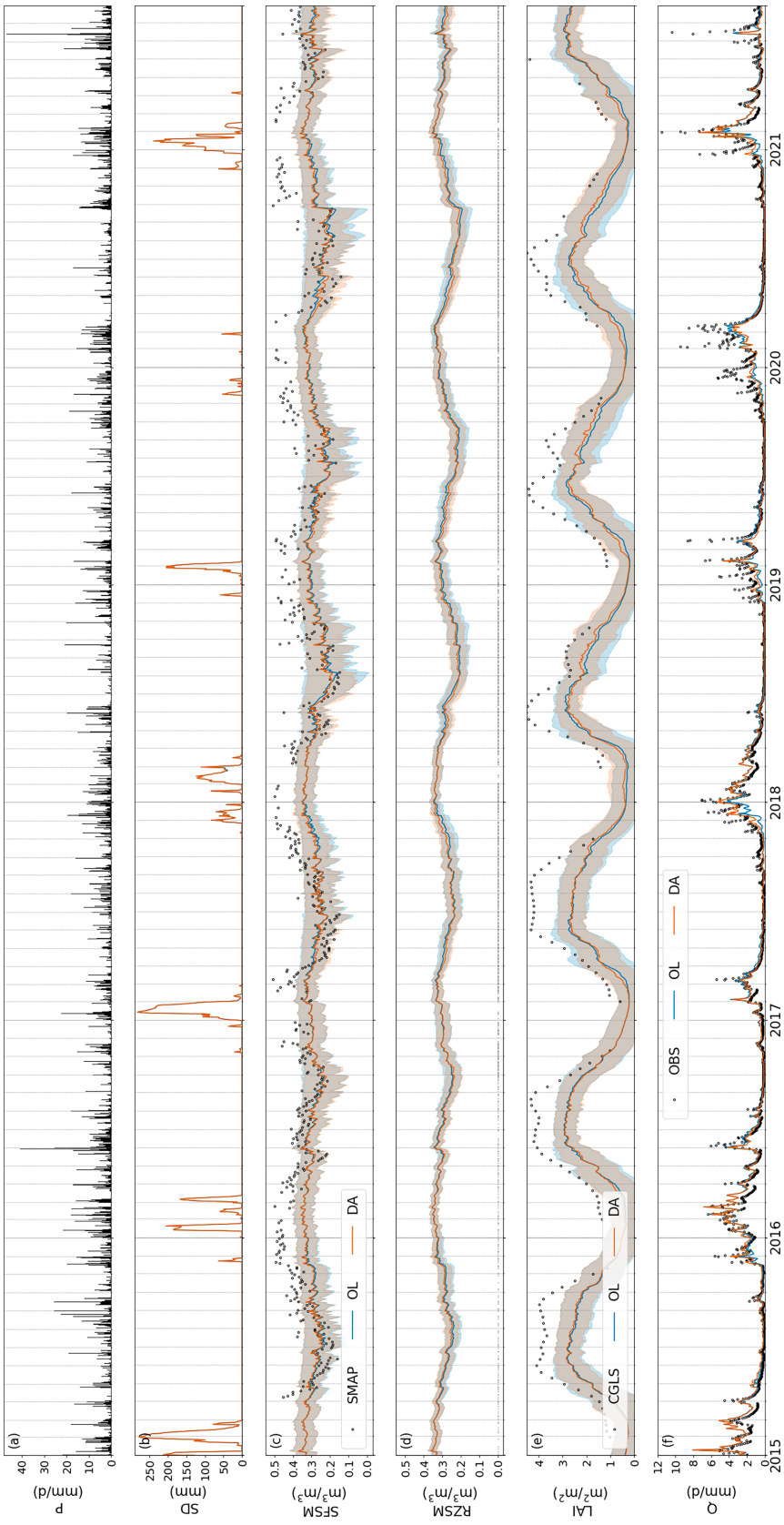


FIG. 11. As in Fig. 10, but for the Ourthe catchment. Note that observed $Q$ on 15 and 16 Jul 2021 was 24 and 21 mm day$^{-1}$, respectively (not shown).

TABLE 2. Kling–Gupta efficiency index (KGE) and KGEsq for daily streamflow at the outlet of the Demer and Ourthe catchments for the different experiments (January 2015–August 2021).

| | KGE (—) | | | KGEsq (—) | | |
|---|---|---|---|---|---|---|
| | OL | DASM | DASMLAI | OL | DASM | DASMLAI |
| Demer | 0.60 | 0.60 | 0.58 | 0.73 | 0.73 | 0.73 |
| Ourthe | 0.59 | 0.62 | 0.62 | 0.80 | 0.83 | 0.83 |

streamflow or based on model (DA) estimates. The antecedent soil moisture estimates always originated from the DA experiment DASM. Figure 14 shows that soil moisture–runoff coupling is substantially higher for the Ourthe catchment than for the Demer catchment for total streamflow as well as for the baseflow and stormflow components individually. For both the Demer and Ourthe catchments, the modeled coupling strength matches well with the observed coupling strength, which was not the case for most models in the intercomparison of Crow et al. (2018). The lower coupling strength in the Demer catchment shows that, naturally, we can already expect a lower impact of soil moisture changes on streamflow estimates there. Possible reasons for the weaker coupling are the different soils in both catchments as well as the higher urban and built-up fraction in the Demer catchment. Over built-up areas, soil moisture obviously does not have any impact because rainfall turns immediately into gridcell runoff that is then routed toward the outlet.

## 6. Conclusions

The added value of Sentinel-1 $\gamma^0$ DA for streamflow estimation was evaluated for two different catchments in Belgium from January 2015 through August 2021. The Demer catchment is dominated by agriculture and mild topography, whereas the Ourthe catchment is largely forested and wetter and colder than the Demer catchment. The DA setup was using the Noah-MP land surface model, the HyMAP routing model, the water cloud model as an observation operator, and an ensemble Kalman filter for state

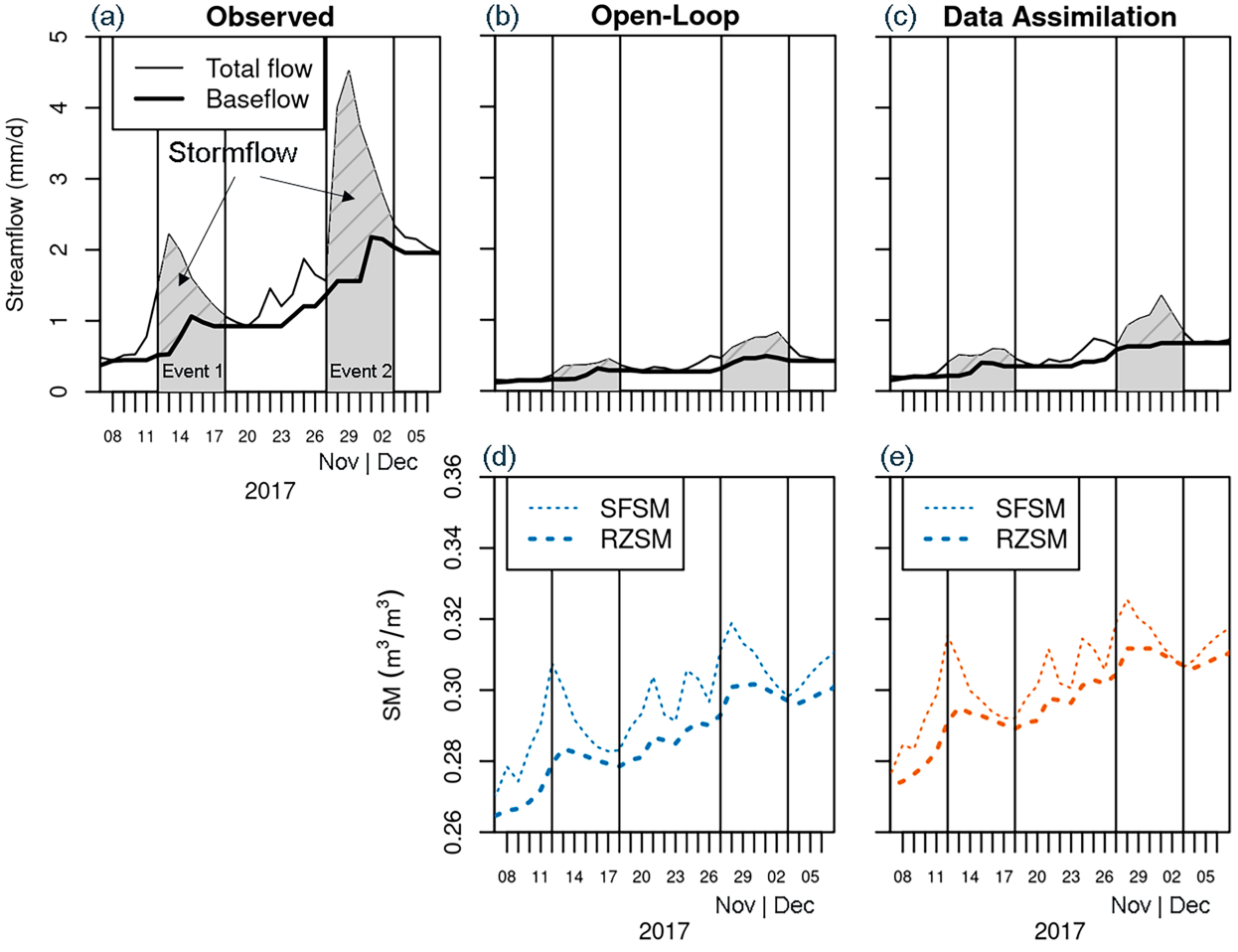


FIG. 12. Example of two identified storm events and the separation of total flow into baseflow and stormflow for (a) observed, (b) open-loop, and (c) DASMLAI streamflow in the Ourthe catchment. (d),(e) The SFSM and RZSM.

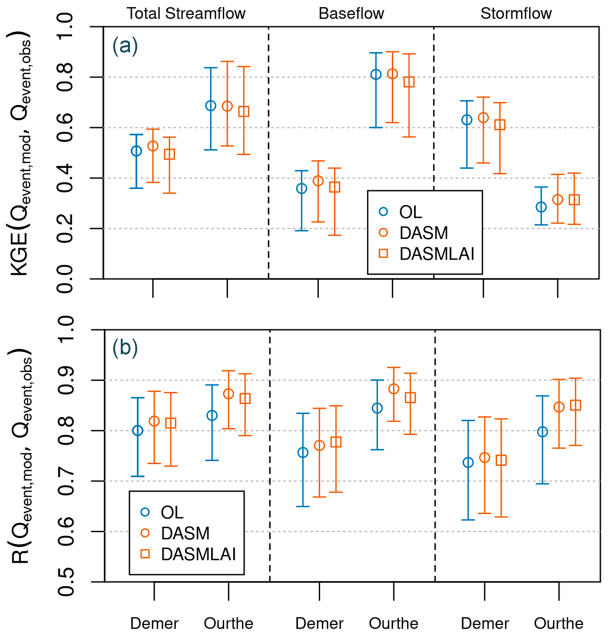


FIG. 13. (a) KGE and (b) Pearson correlation coefficients $R$ (with 95% confidence intervals) between event-scale modeled ($Q_{event,mod}$) and observed ($Q_{event,obs}$) streamflow, for (left) total streamflow, (center) baseflow, and (right) stormflow (Demer: $n = 88$; Ourthe: $n = 72$).

updating. For this setup, our results support the following conclusions:

- the assimilation of Sentinel-1 $\gamma^0$ observations can correct SFSM for rainfall errors and improve SFSM estimates based on a comparison against independent satellite-based SFSM retrievals;
- the presence of forest cover does not seem to prohibit the assimilation of Sentinel-1 $\gamma^0$ as suggested by multiple promising evaluation metrics over the Ourthe catchment;
- the simultaneous updating of soil moisture and LAI could not be shown to be superior to updating soil moisture only, which might be caused by deficiencies of the water cloud model and the strong tendency of the Noah-MP vegetation model to drift back toward its model equilibrium state;
- the improved soil moisture through Sentinel-1 DA can improve streamflow estimates if both the observational data and the model show a strong soil moisture–runoff coupling, which was the case only for the Ourthe catchment; and
- with an ensemble Kalman filter for state updating like used in this study, improvements are largely limited to dynamical metrics such as correlation, while bias remains mostly unaffected.

Increasing the physical realism of the process model is supposed to increase the positive impacts of the presented backscatter data assimilation on streamflow estimation. Newer model input (e.g., newer soil maps; Poggio et al. 2021), improved model structure (Vereecken et al. 2019), and parameter calibration

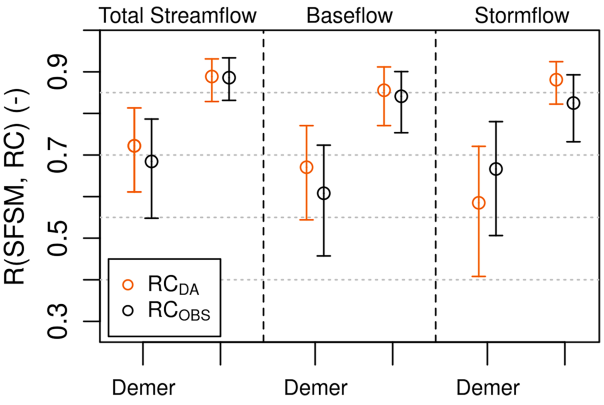


FIG. 14. Values of Spearman correlation coefficient $R$ (with 95% confidence intervals) between SFSM and runoff coefficient (RC) of total streamflow, baseflow, and stormflow. SFSM is derived from the DASM experiment. $RC_{DA}$ is calculated with simulated streamflow and MERRA-2 precipitation, whereas $RC_{OBS}$ is calculated with measured streamflow and rain gauge data.

(Crow et al. 2018) are needed to reduce bias and peak flow timing offsets and to ensure that improved soil moisture optimally propagates into improved streamflow estimates. Additionally, remaining systematic model errors can further be addressed directly by the data assimilation setup through parameter updating. Additionally, remaining systematic model errors can further be addressed directly by the data assimilation setup through parameter updating. While this study analyzed two catchments in detail, several more catchments with diverse properties would need to be investigated to generalize these conclusions. This will require the consideration of additional factors like regional differences in, e.g., climate, vegetation, and agricultural practices.

*Acknowledgments.* This study was funded by the Belgian Science Policy Office (BELSPO STEREO 3 Project SR/00/376 EO-DAHR). The computer resources and services used in this work were provided by the High-Performance Computing system of the Vlaams Supercomputer Center, funded by the Research Foundation—Flanders (FWO) and the Flemish Government (Storage4Climate collaborative grant). We thank Guillaume Thirel and Sarah Dance for valuable feedback on the conducted research.

*Data availability statement.* The source code used for the Sentinel-1 backscatter data assimilation within NASA LIS is publicly accessible at https://github.com/NASA-LIS/LISF/pull/1208/. The conducted simulation experiments were performed on the Vlaams Supercomputer Center high-performance computing platform, and model output is available from https://doi.org/10.5281/zenodo.10170739. The rain gauge and streamflow data were retrieved from www.waterinfo.be and https://hydrometrie.wallonie.be. The MERRA-2 dataset was retrieved from https://goldsmr4.gesdisc.eosdis.nasa.gov/data/MERRA2. The Sentinel-1 dataset was retrieved from http://sentinel1-slc-seasia-pds.s3-website-ap-southeast-1.amazonaws.com/datasets/slc/v1.1.

## REFERENCES


Albergel, C., and Coauthors, 2017: Sequential assimilation of satellite-derived vegetation and soil moisture products using SURFEX-v8.0: LDAS-Monde assessment over the Euro-Mediterranean area. *Geosci. Model Dev.*, **10**, 3889–3912, https://doi.org/10.5194/gmd-10-3889-2017.

Attema, E. P. W., and F. T. Ulaby, 1978: Vegetation modeled as a water cloud. *Radio Sci.*, **13**, 357–364, https://doi.org/10.1029/RS013i002p00357.

Ball, J. T., I. E. Woodrow, and J. A. Berry, 1987: A model predicting stomatal conductance and its contribution to the control of photosynthesis under different environmental conditions. *Progress in Photosynthesis Research*, Springer, 221–224, https://doi.org/10.1007/978-94-017-0519-6_48.

Berthet, L., V. Andréassian, C. Perrin, and P. Javelle, 2009: How crucial is it to account for the antecedent moisture conditions in flood forecasting? Comparison of event-based and continuous approaches on 178 catchments. *Hydrol. Earth Syst. Sci.*, **13**, 819–831, https://doi.org/10.5194/hess-13-819-2009.

Cenci, L., L. Pulvirenti, G. Boni, M. Chini, P. Matgen, S. Gabellani, G. Squicciarino, and N. Pierdicca, 2017: An evaluation of the potential of Sentinel 1 for improving flash flood predictions via soil moisture–data assimilation. *Adv. Geosci.*, **44**, 89–100, https://doi.org/10.5194/adgeo-44-89-2017.

Chan, S. K., and Coauthors, 2018: Development and assessment of the SMAP enhanced passive soil moisture product. *Remote Sens. Environ.*, **204**, 931–941, https://doi.org/10.1016/j.rse.2017.08.025.

Chaubell, M. J., and Coauthors, 2020: Improved SMAP dual-channel algorithm for the retrieval of soil moisture. *IEEE Trans. Geosci. Remote Sens.*, **58**, 3894–3905, https://doi.org/10.1109/TGRS.2019.2959239.

Chen, F., and Coauthors, 1996: Modeling of land surface evaporation by four schemes and comparison with FIFE observations. *J. Geophys. Res.*, **101**, 7251–7268, https://doi.org/10.1029/95JD02165.

——, W. T. Crow, P. J. Starks, and D. N. Moriasi, 2011: Improving hydrologic predictions of a catchment model via assimilation of surface soil moisture. *Adv. Water Resour.*, **34**, 526–536, https://doi.org/10.1016/j.advwatres.2011.01.011.

Cosgrove, B. A., and Coauthors, 2003: Real-time and retrospective forcing in the North American Land Data Assimilation System (NLDAS) project. *J. Geophys. Res.*, **108**, 8842, https://doi.org/10.1029/2002JD003118.

Crow, W. T., F. Chen, R. H. Reichle, Y. Xia, and Q. Liu, 2018: Exploiting soil moisture, precipitation, and streamflow observations to evaluate soil moisture/runoff coupling in land surface models. *Geophys. Res. Lett.*, **45**, 4869–4878, https://doi.org/10.1029/2018GL077193.

Decharme, B., and Coauthors, 2019: Recent changes in the ISBA-CTRIP land surface system for use in the CNRM-CM6 climate model and in global off-line hydrological applications. *J. Adv. Model. Earth Syst.*, **11**, 1207–1252, https://doi.org/10.1029/2018MS001545.

Dee, D. P., 2005: Bias and data assimilation. *Quart. J. Roy. Meteor. Soc.*, **131**, 3323–3343, https://doi.org/10.1256/qj.05.137.

De Lannoy, G. J. M., and R. H. Reichle, 2016a: Assimilation of SMOS brightness temperatures or soil moisture retrievals into a land surface model. *Hydrol. Earth Syst. Sci.*, **20**, 4895–4911, https://doi.org/10.5194/hess-20-4895-2016.

——, and ——, 2016b: Global assimilation of multiangle and multipolarization SMOS brightness temperature observations into the GEOS-5 catchment land surface model for soil moisture estimation. *J. Hydrometeor.*, **17**, 669–691, https://doi.org/10.1175/JHM-D-15-0037.1.

——, ——, P. R. Houser, V. R. N. Pauwels, and N. E. C. Verhoest, 2007: Correcting for forecast bias in soil moisture assimilation with the ensemble Kalman filter. *Water Resour. Res.*, **43**, W09410, https://doi.org/10.1029/2006WR005449.

——, R. D. Koster, R. H. Reichle, S. P. P. Mahanama, and Q. Liu, 2014: An updated treatment of soil texture and associated hydraulic properties in a global land modeling system. *J. Adv. Model. Earth Syst.*, **6**, 957–979, https://doi.org/10.1002/2014MS000330.

——, and Coauthors, 2022: Perspective on satellite-based land data assimilation to estimate water cycle components in an era of advanced data availability and model sophistication. *Front. Water*, **4**, 981745, https://doi.org/10.3389/frwa.2022.981745.

de Rosnay, P., G. Balsamo, C. Albergel, J. Muñoz-Sabater, and L. Isaksen, 2014: Initialisation of land surface variables for numerical weather prediction. *Surv. Geophys.*, **35**, 607–621, https://doi.org/10.1007/s10712-012-9207-x.

De Santis, D., D. Biondi, W. T. Crow, S. Camici, S. Modanesi, L. Brocca, and C. Massari, 2021: Assimilation of satellite soil moisture products for river flow prediction: An extensive experiment in over 700 catchments throughout Europe. *Water Resour. Res.*, **57**, e2021WR029643, https://doi.org/10.1029/2021WR029643.

Dickinson, R. E., A. Henderson-Sellers, and P. J. Kennedy, 1993: Biosphere-Atmosphere Transfer Scheme (BATS) version 1e as coupled to the NCAR Community Climate Model. NCAR Tech. Note NCAR/TN-387+STR, 80 pp., http://n2t.net/ark:/85065/d7ns0t8g.

——, M. Shaikh, R. Bryant, and L. Graumlich, 1998: Interactive canopies for a climate model. *J. Climate*, **11**, 2823–2836, https://doi.org/10.1175/1520-0442(1998)011<2823:ICFACM>2.0.CO;2.

Duan, Q. Y., V. K. Gupta, and S. Sorooshian, 1993: Shuffled complex evolution approach for effective and efficient global minimization. *J. Optim. Theory Appl.*, **76**, 501–521, https://doi.org/10.1007/BF00939380.

Fairbairn, D., A. Lavinia Barbu, A. Napoly, C. Albergel, J.-F. Mahfouf, and J.-C. Calvet, 2017: The effect of satellite-derived surface soil moisture and leaf area index land data assimilation on streamflow simulations over France. *Hydrol. Earth Syst. Sci.*, **21**, 2015–2033, https://doi.org/10.5194/hess-21-2015-2017.

FAO/IIASA/ISRIC/ISSCAS/JRC, 2012: Harmonized World Soil Database (version 1.21). FAO and IIASA, accessed 30 October 2017, http://webarchive.iiasa.ac.at/Research/LUC/External-World-soil-database/HTML/.

Farr, T. G., and Coauthors, 2007: The Shuttle Radar Topography Mission. *Rev. Geophys.*, **45**, RG2004, https://doi.org/10.1029/2005RG000183.

Friedl, M. A., and Coauthors, 2002: Global land cover mapping from MODIS: Algorithms and early results. *Remote Sens. Environ.*, **83**, 287–302, https://doi.org/10.1016/S0034-4257(02)00078-0.

Gelaro, R., and Coauthors, 2017: The Modern-Era Retrospective Analysis for Research and Applications, version 2 (MERRA-2). *J. Climate*, **30**, 5419–5454, https://doi.org/10.1175/JCLI-D-16-0758.1.

Getirana, A. C. V., and C. Peters-Lidard, 2013: Estimating water discharge from large radar altimetry datasets. *Hydrol. Earth Syst. Sci.*, **17**, 923–933, https://doi.org/10.5194/hess-17-923-2013.

——, A. Boone, D. Yamazaki, B. Decharme, F. Papa, and N. Mognard, 2012: The Hydrological Modeling and Analysis

Platform (HyMAP): Evaluation in the Amazon basin. *J. Hydrometeor.*, **13**, 1641–1665, https://doi.org/10.1175/JHM-D-12-021.1.

——, C. Peters-Lidard, M. Rodell, and P. D. Bates, 2017: Trade-off between cost and accuracy in large-scale surface water dynamic modeling. *Water Resour. Res.*, **53**, 4942–4955, https://doi.org/10.1002/2017WR020519.

——, S. V. Kumar, G. Konapala, and C. E. Ndehedehe, 2021: Impacts of fully coupling land surface and flood models on the simulation of large wetlands' water dynamics: The case of the inner Niger delta. *J. Adv. Model. Earth Syst.*, **13**, e2021MS002463, https://doi.org/10.1029/2021MS002463.

Gupta, H. V., H. Kling, K. K. Yilmaz, and G. F. Martinez, 2009: Decomposition of the mean squared error and NSE performance criteria: Implications for improving hydrological modelling. *J. Hydrol.*, **377**, 80–91, https://doi.org/10.1016/j.jhydrol.2009.08.003.

Hansen, M. C., R. S. Defries, J. R. G. Townshend, and R. Sohlberg, 2000: Global land cover classification at 1 km spatial resolution using a classification tree approach. *Int. J. Remote Sens.*, **21**, 1331–1364, https://doi.org/10.1080/014311600210209.

Janjić, T., and Coauthors, 2018: On the representation error in data assimilation. *Quart. J. Roy. Meteor. Soc.*, **144**, 1257–1278, https://doi.org/10.1002/qj.3130.

Kumar, S. V., and Coauthors, 2006: Land information system: An interoperable framework for high resolution land surface modeling. *Environ. Modell. Software*, **21**, 1402–1415, https://doi.org/10.1016/j.envsoft.2005.07.004.

——, D. M. Mocko, S. Wang, C. D. Peters-Lidard, and J. Borak, 2019: Assimilation of remotely sensed leaf area index into the Noah-MP land surface model: Impacts on water and carbon fluxes and states over the continental United States. *J. Hydrometeor.*, **20**, 1359–1377, https://doi.org/10.1175/JHM-D-18-0237.1.

——, and Coauthors, 2021: The 2019–2020 Australian drought and bushfires altered the partitioning of hydrological fluxes. *Geophys. Res. Lett.*, **48**, e2020GL091411, https://doi.org/10.1029/2020GL091411.

Lievens, H., and Coauthors, 2017: Joint Sentinel-1 and SMAP data assimilation to improve soil moisture estimates. *Geophys. Res. Lett.*, **44**, 6145–6153, https://doi.org/10.1002/2017GL073904.

——, I. Brangers, H.-P. Marshall, T. Jonas, M. Olefs, and G. De Lannoy, 2022: Sentinel-1 snow depth retrieval at sub-kilometer resolution over the European Alps. *Cryosphere*, **16**, 159–177, https://doi.org/10.5194/tc-16-159-2022.

Liu, X., F. Chen, M. Barlage, G. Zhou, and D. Niyogi, 2016: Noah-MP-Crop: Introducing dynamic crop growth in the Noah-MP land surface model. *J. Geophys. Res.*, **121**, 13 953–13 972, https://doi.org/10.1002/2016JD025597.

Liu, Y., W. Wang, and Y. Liu, 2018: ESA CCI soil moisture assimilation in SWAT for improved hydrological simulation in upper Huai River basin. *Adv. Meteor.*, **2018**, 7301314, https://doi.org/10.1155/2018/7301314.

Loizu, J., C. Massari, J. Álvarez-Mozos, A. Tarpanelli, L. Brocca, and J. Casalí, 2018: On the assimilation set-up of ASCAT soil moisture data for improving streamflow catchment simulation. *Adv. Water Resour.*, **111**, 86–104, https://doi.org/10.1016/j.advwatres.2017.10.034.

Mao, Y., W. T. Crow, and B. Nijssen, 2019: A framework for diagnosing factors degrading the streamflow performance of a soil moisture data assimilation system. *J. Hydrometeor.*, **20**, 79–97, https://doi.org/10.1175/JHM-D-18-0115.1.

Mirus, B. B., and K. Loague, 2013: How runoff begins (and ends): Characterizing hydrologic response at the catchment scale. *Water Resour. Res.*, **49**, 2987–3006, https://doi.org/10.1002/wrcr.20218.

Modanesi, S., C. Massari, A. Gruber, H. Lievens, A. Tarpanelli, R. Morbidelli, and G. J. M. De Lannoy, 2021: Optimizing a backscatter forward operator using Sentinel-1 data over irrigated land. *Hydrol. Earth Syst. Sci.*, **25**, 6283–6307, https://doi.org/10.5194/hess-25-6283-2021.

——, ——, M. Bechtold, H. Lievens, A. Tarpanelli, L. Brocca, L. Zappa, and G. J. M. De Lannoy, 2022: Challenges and benefits of quantifying irrigation through the assimilation of Sentinel-1 backscatter observations into Noah-MP. *Hydrol. Earth Syst. Sci.*, **26**, 4685–4706, https://doi.org/10.5194/hess-26-4685-2022.

Moramarco, T., C. Pandolfo, and V. P. Singh, 2008: Accuracy of kinematic wave and diffusion wave approximations for flood routing. I: Steady analysis. *J. Hydrol. Eng.*, **13**, 1078–1088, https://doi.org/10.1061/(ASCE)1084-0699(2008)13:11(1078).

Niu, G.-Y., Z.-L. Yang, R. E. Dickinson, and L. E. Gulden, 2005: A simple TOPMODEL-based runoff parameterization (SIMTOP) for use in global climate models. *J. Geophys. Res.*, **110**, D21106, https://doi.org/10.1029/2005JD006111.

——, ——, ——, ——, and H. Su, 2007: Development of a simple groundwater model for use in climate models and evaluation with gravity recovery and climate experiment data. *J. Geophys. Res.*, **112**, D07103, https://doi.org/10.1029/2006JD007522.

——, and Coauthors, 2011: The community Noah land surface model with multiparameterization options (Noah-MP): 1. Model description and evaluation with local-scale measurements. *J. Geophys. Res.*, **116**, D12109, https://doi.org/10.1029/2010JD015139.

Pauwels, V. R. N., R. Hoeben, N. E. C. Verhoest, and F. P. De Troch, 2001: The importance of the spatial patterns of remotely sensed soil moisture in the improvement of discharge predictions for small-scale basins through data assimilation. *J. Hydrol.*, **251**, 88–102, https://doi.org/10.1016/S0022-1694(01)00440-1.

Penna, D., H. J. Tromp-van Meerveld, A. Gobbi, M. Borga, and G. Dalla Fontana, 2011: The influence of soil moisture on threshold runoff generation processes in an alpine headwater catchment. *Hydrol. Earth Syst. Sci.*, **15**, 689–702, https://doi.org/10.5194/hess-15-689-2011.

Peters-Lidard, C. D., and Coauthors, 2007: High-performance Earth system modeling with NASA/GSFC's Land Information System. *Innovations Syst. Software Eng.*, **3**, 157–165, https://doi.org/10.1007/s11334-007-0028-x.

Poggio, L., L. M. De Sousa, N. H. Batjes, G. B. M. Heuvelink, B. Kempen, E. Ribeiro, and D. Rossiter, 2021: SoilGrids 2.0: Producing soil information for the globe with quantified spatial uncertainty. *Soil*, **7**, 217–240, https://doi.org/10.5194/soil-7-217-2021.

Quast, R., and W. Wagner, 2016: Analytical solution for first-order scattering in bistatic radiative transfer interaction problems of layered media. *Appl. Opt.*, **55**, 5379–5386, https://doi.org/10.1364/AO.55.005379.

Radatz, T. F., A. M. Thompson, and F. W. Madison, 2013: Soil moisture and rainfall intensity thresholds for runoff generation in southwestern Wisconsin agricultural watersheds. *Hydrol. Processes*, **27**, 3521–3534, https://doi.org/10.1002/hyp.9460.

Reichle, R. H., J. P. Walker, R. D. Koster, and P. R. Houser, 2002: Extended versus ensemble Kalman filtering for land data assimilation. *J. Hydrometeor.*, **3**, 728–740, https://doi.org/10.1175/1525-7541(2002)003<0728:EVEKFF>2.0.CO;2.

——, and Coauthors, 2017a: Global assessment of the SMAP level-4 surface and root-zone soil moisture product using

assimilation diagnostics. *J. Hydrometeor.*, **18**, 3217–3237, https://doi.org/10.1175/JHM-D-17-0130.1.

——, Q. Liu, R. D. Koster, C. S. Draper, S. P. P. Mahanama, and G. S. Partyka, 2017b: Land surface precipitation in MERRA-2. *J. Climate*, **30**, 1643–1664, https://doi.org/10.1175/JCLI-D-16-0570.1.

——, ——, J. V. Ardizzone, W. T. Crow, G. J. M. De Lannoy, J. Dong, J. S. Kimball, and R. D. Koster, 2021: The contributions of gauge-based precipitation and SMAP brightness temperature observations to the skill of the SMAP level-4 soil moisture product. *J. Hydrometeor.*, **22**, 405–424, https://doi.org/10.1175/JHM-D-20-0217.1.

Ryu, D., W. T. Crow, X. Zhan, and T. J. Jackson, 2009: Correcting unintended perturbation biases in hydrologic data assimilation. *J. Hydrometeor.*, **10**, 734–750, https://doi.org/10.1175/2008JHM1038.1.

Sabater, J. M., C. Rüdiger, J.-C. Calvet, N. Fritz, L. Jarlan, and Y. Kerr, 2008: Joint assimilation of surface soil moisture and LAI observations into a land surface model. *Agric. For. Meteor.*, **148**, 1362–1373, https://doi.org/10.1016/j.agrformet.2008.04.003.

Scherrer, S., G. De Lannoy, Z. Heyvaert, M. Bechtold, C. Albergel, T. S. El Madany, and W. Dorigo, 2022: Effects of a biased LAI data assimilation system on hydrological variables and carbon uptake over Europe. *EGUsphere*, https://doi.org/10.5194/egusphere-2022-1137.

Schlund, M., and S. Erasmi, 2020: Sentinel-1 time series data for monitoring the phenology of winter wheat. *Remote Sens. Environ.*, **246**, 111814, https://doi.org/10.1016/j.rse.2020.111814.

Sloto, R. A., and M. Y. Crouse, 1996: HYSEP: A computer program for streamflow hydrograph separation and analysis. USGS Water-Resources Investigations Rep. 96-4040, 51 pp., https://pubs.usgs.gov/wri/1996/4040/report.pdf.

Torres, R., 2002: A threshold condition for soil-water transport. *Hydrol. Processes*, **16**, 2703–2706, https://doi.org/10.1002/hyp.5060.

Tramblay, Y., C. Bouvier, C. Martin, J.-F. Didon-Lescot, D. Todorovik, and J.-M. Domergue, 2010: Assessment of initial soil moisture conditions for event-based rainfall–runoff modelling. *J. Hydrol.*, **387**, 176–187, https://doi.org/10.1016/j.jhydrol.2010.04.006.

Ulaby, F. T., P. P. Batlivala, and M. C. Dobson, 1978: Microwave backscatter dependence on surface roughness, soil moisture, and soil texture: Part I—Bare soil. *IEEE Trans. Geosci. Electron.*, **16**, 286–295, https://doi.org/10.1109/TGE.1978.294586.

van Leeuwen, P. J., 2015: Representation errors and retrievals in linear and nonlinear data assimilation. *Quart. J. Roy. Meteor. Soc.*, **141**, 1612–1623, https://doi.org/10.1002/qj.2464.

Vereecken, H., and Coauthors, 2019: Infiltration from the pedon to global grid scales: An overview and outlook for land surface modeling. *Vadose Zone J.*, **18**, 180191, https://doi.org/10.2136/vzj2018.10.0191.

Verger, A., F. Baret, and M. Weiss, 2014: Near real-time vegetation monitoring at global scale. *IEEE J. Sel. Top. Appl. Earth Obs. Remote Sens.*, **7**, 3473–3481, https://doi.org/10.1109/JSTARS.2014.2328632.

Vreugdenhil, M., W. Wagner, B. Bauer-Marschallinger, I. Pfeil, I. Teubner, C. Rüdiger, and P. Strauss, 2018: Sensitivity of Sentinel-1 backscatter to vegetation dynamics: An Austrian case study. *Remote Sens.*, **10**, 1396, https://doi.org/10.3390/rs10091396.

——, C. Navacchi, B. Bauer-Marschallinger, S. Hahn, S. Steele-Dunne, I. Pfeil, W. Dorigo, and W. Wagner, 2020: Sentinel-1 cross ratio and vegetation optical depth: A comparison over Europe. *Remote Sens.*, **12**, 3404, https://doi.org/10.3390/rs12203404.

Wanders, N., D. Karssenberg, A. de Roo, S. M. de Jong, and M. F. P. Bierkens, 2014: The suitability of remotely sensed soil moisture for improving operational flood forecasting. *Hydrol. Earth Syst. Sci.*, **18**, 2343–2357, https://doi.org/10.5194/hess-18-2343-2014.

Wigneron, J.-P., and Coauthors, 2007: L-band Microwave Emission of the Biosphere (L-MEB) model: Description and calibration against experimental data sets over crop fields. *Remote Sens. Environ.*, **107**, 639–655, https://doi.org/10.1016/j.rse.2006.10.014.

——, and Coauthors, 2017: Modelling the passive microwave signature from land surfaces: A review of recent results and application to the L-band SMOS & SMAP soil moisture retrieval algorithms. *Remote Sens. Environ.*, **192**, 238–262, https://doi.org/10.1016/j.rse.2017.01.024.

Winter, T. C., 2007: The role of ground water in generating streamflow in headwater areas and in maintaining base flow. *J. Amer. Water Resour. Assoc.*, **43**, 15–25, https://doi.org/10.1111/j.1752-1688.2007.00003.x.

Xu, T., F. Chen, X. He, M. Barlage, Z. Zhang, S. Liu, and X. He, 2021: Improve the performance of the Noah-MP-Crop model by jointly assimilating soil moisture and vegetation phenology data. *J. Adv. Model. Earth Syst.*, **13**, e2020MS002394, https://doi.org/10.1029/2020MS002394.

Yamazaki, D., and Coauthors, 2017: A high-accuracy map of global terrain elevations. *Geophys. Res. Lett.*, **44**, 5844–5853, https://doi.org/10.1002/2017GL072874.

Zomlot, Z., B. Verbeiren, M. Huysmans, and O. Batelaan, 2015: Spatial distribution of groundwater recharge and base flow: Assessment of controlling factors. *J. Hydrol. Reg. Stud.*, **4**, 349–368, https://doi.org/10.1016/j.ejrh.2015.07.005.